
Entropic (Gromov) Wasserstein Flow Matching with GENOT

Dominik Klein^{*1†} Théo Uscidda^{*2} Fabian J. Theis¹ Marco Cuturi³

Abstract

Optimal transport (OT) theory has reshaped the field of generative modeling: Combined with neural networks, recent *Neural OT* (N-OT) solvers use OT as an inductive bias, to focus on “thrifty” mappings that minimize average displacement costs. This core principle has fueled the successful application of N-OT solvers to high-stakes scientific challenges, notably single-cell genomics. N-OT solvers are, however, increasingly confronted with practical challenges: while most N-OT solvers can handle squared-Euclidean costs, they must be repurposed to handle more general costs; their reliance on deterministic Monge maps as well as mass conservation constraints can easily go awry in the presence of outliers; mapping points *across* heterogeneous spaces is out of their reach. While each of these challenges has been explored independently, we propose a new framework that can handle, natively, all of these needs. The *generative entropic neural OT* (GENOT) framework models the conditional distribution $\pi_\varepsilon(\mathbf{y}|\mathbf{x})$ of an optimal *entropic* coupling π_ε , using conditional flow matching. GENOT is generative, and can transport points *across* spaces, guided by sample-based, unbalanced solutions to the Gromov-Wasserstein problem, that can use any cost. We showcase our approach on both synthetic and single-cell datasets, using GENOT to model cell development, predict cellular responses, and translate between data modalities.

1. Introduction

Mapping a probability distribution onto another is a ubiquitous challenge in machine learning, with many implications in generative modeling. Optimal transport (OT) has arisen in a few years as a major purveyor of tools to better address these challenges, both in theory and practice. OT

focuses on finding maps that can effectively transform a distribution of matter onto another, by minimizing a certain notion of cost (Santambrogio, 2015). Applying OT to large-dimensional problems arising in machine learning and sciences has necessitated various modifications and adaptations. Starting with solvers that can solve approximate matching problems at large scales (Cuturi, 2013; Peyré et al., 2016; Scetbon et al., 2021; 2022), a recent plethora of OT-inspired training approaches for neural networks have been proposed (Makkuva et al., 2020; Korotin et al., 2020; Asadulaev et al., 2022; Fan et al., 2020; Uscidda & Cuturi, 2023; Lipman et al., 2023; Tong et al., 2020; 2023b). Mirroring these new possibilities in the field of single-cell genomics, arguably one of the most exciting transfers of OT to science, the use of OT has evolved from point-wise matching problems (Schiebinger et al., 2019; Demetci et al., 2022), to neural-based approaches that can, for instance, predict the response of cells to various perturbations (Bunne et al., 2021; 2022). As a testament of their success, practitioners demand ever more flexibility from Neural-OT solvers, in a suite of increasingly complex challenges:

From Deterministic to Stochastic Maps. The classic OT pipeline rests on deterministic (Monge) maps. Such maps lack flexibility, both at estimation and inference time. Practitioners may favor, instead, stochasticity, which would account naturally for instance, for the non-determinism of cell evolutions (Elowitz et al., 2002). Stochastic formulations can also produce a conditional distribution that can be used to quantify uncertainty. In the discrete setting, this property is fulfilled by entropy-regularized OT (EOT) (Cuturi, 2013). In a neural setting, some works (Korotin et al., 2022; 2023b; Asadulaev et al., 2022) have explored computing weak OT coupling by solving a min-max problem.

From Linear to Quadratic Problems. Classic “linear” OT puts in correspondence distributions defined in the same space \mathcal{X} , using a cost $c(\mathbf{x}, \mathbf{y})$ for any two points $\mathbf{x}, \mathbf{y} \in \mathcal{X}$ (most often set to be the squared Euclidean distance (Santambrogio, 2015, §1.3) in applications). Yet, more challenging use-cases arising in practice now involve source and target distributions that do *not* live in the same space, e.g. \mathcal{X} and \mathcal{Y} have differing dimensions, as in Demetci et al. (2022). The challenge, in that case, lies in the absence of a “natural” cost function between vectors of different sizes. This can be bypassed using *quadratic* losses (Mémoli, 2011;

^{*}Equal contribution [†]Work done during internship at Apple
¹Helmholtz Munich & TU Munich, Germany ²CREST-ENSAE, Germany ³Apple, Paris, France. Correspondence to: Marco Cuturi <marco.cuturi@apple.com>.

Sturm, 2020), a.k.a. Gromov-Wasserstein (GW) problems. Despite the challenges inherent to solving GW, practitioners have expressed much interest in that flexibility, as evidenced by the wide adoption of the mixed linear/quadratic fused Gromov-Wasserstein (FGW) distance (Vayer et al., 2018), see e.g. Klein et al. (2023); Lange et al. (2023); Nitzan et al. (2019); Zeira et al. (2022). To our knowledge, the only neural formulation for GW proposed thus far by (Nekrashevich et al., 2023) learns deterministic maps for the inner product costs, using a min-max-min optimization procedure.

Flexibility in Mass Conservation. In many real-world applications, the data acquisition process can be error-prone, resulting in outliers. To mitigate this, unbalanced OT (UOT) formulations that can discard observations have been proposed (Frogner et al., 2015; Chizat et al., 2018; Séjourné et al., 2021), with numerous applications to generative modeling (Balaji et al., 2020; Yang & Uhler, 2019; Eyring et al., 2023) and single-cell genomics (Schiebinger et al., 2019; Eyring et al., 2022; Lübeck et al., 2022).

Contributions. We propose a flexible neural OT framework that satisfies all the requirements above:

- We propose GENOT, the first method that parameterizes linear and quadratic EOT couplings by modeling their conditional distributions with neural networks (Prop. 3.1), using flow matching (Lipman et al., 2023) as a core block, and *any* cost function between samples.
- By showing that an unbalanced EOT problem is equivalent to a balanced one between re-weighted measures (Prop. 3.2), that can be estimated consistently (Prop. 3.3), we introduce U-GENOT to solve unbalanced problems.
- We extend (U-)GENOT to solve the fused problem (§ 3.3). To our knowledge, GENOT is the first method to solve a continuous fused problem.
- We show that GENOT outperforms other linear neural EOT solvers on the Gushchin et al. (2023) benchmark,
- We showcase GENOT’s ability to handle crucial single-cell biology challenges: we (i) quantify lineage branching events in the developing mouse pancreas, (ii) predict cellular responses to drug perturbations, along with a well-calibrated uncertainty estimation, and (iii) introduce a novel method to translate ATAC-seq to RNA-seq data.

2. Background

Notations. We consider in this work two compact sets $\mathcal{X} \subset \mathbb{R}^p$, $\mathcal{Y} \subset \mathbb{R}^q$, referred to as the source and the target domain, respectively. In general, $p \neq q$. The set of positive (resp. probability) measures on \mathcal{X} is denoted by $\mathcal{M}^+(\mathcal{X})$ (resp. $\mathcal{M}_1^+(\mathcal{X})$). For $\pi \in \mathcal{M}^+(\mathcal{X} \times \mathcal{Y})$, $\pi_1 := p_1 \# \pi$ and $\pi_2 := p_2 \# \pi$ denote its marginals. Then, for $\mu \in \mathcal{M}^+(\mathcal{X})$, $\nu \in \mathcal{M}^+(\mathcal{Y})$, $\Pi(\mu, \nu) = \{\pi : \pi_1 = \mu, \pi_2 = \nu\}$. Moreover, $\frac{d\mu}{d\nu}$ denotes the relative density of

μ w.r.t. ν , and we write $\mu = \frac{d\mu}{d\nu} \cdot \nu$. For $\rho, \gamma \in \mathcal{M}^+(\mathcal{X})$, $\text{KL}(\rho|\gamma) = \int_{\mathcal{X}} \log\left(\frac{d\rho}{d\gamma}\right) d\rho - \int_{\mathcal{X}} d\gamma + \int_{\mathcal{X}} d\rho$.

Linear Entropic OT. Let $c : \mathcal{X} \times \mathcal{Y} \rightarrow \mathbb{R}$ be a cost function, $\mu \in \mathcal{M}_1^+(\mathcal{X})$, $\nu \in \mathcal{M}_1^+(\mathcal{Y})$ and $\varepsilon \geq 0$. The linear entropy-regularized OT problem reads

$$\min_{\pi \in \Pi(\mu, \nu)} \int_{\mathcal{X} \times \mathcal{Y}} c d\pi + \varepsilon \text{KL}(\pi|\mu \otimes \nu). \quad (\text{LEOT})$$

(LEOT) is also known as the static Schrödinger bridge (SB) problem (Léonard, 2013). With $\varepsilon = 0$, we recover the Kantorovich (1942) problem. When μ and ν are discrete, we can solve (LEOT) with the Sinkhorn algorithm (Cuturi, 2013). For measures on n points, its complexity is $\mathcal{O}(n^2)$ in time, and $\mathcal{O}(n)$ or $\mathcal{O}(n^2)$ in memory, depending on c .

Quadratic Entropic OT. As opposed to considering an *inter-domain* cost defined on $\mathcal{X} \times \mathcal{Y}$, quadratic entropic OT is concerned with seeking couplings based on *intra-domain* cost functions $c_{\mathcal{X}} : \mathcal{X} \times \mathcal{X} \rightarrow \mathbb{R}$ and $c_{\mathcal{Y}} : \mathcal{Y} \times \mathcal{Y} \rightarrow \mathbb{R}$:

$$\min_{\pi \in \Pi(\mu, \nu)} \int_{(\mathcal{X} \times \mathcal{Y})^2} Q_{c_{\mathcal{X}}, c_{\mathcal{Y}}} d(\pi \otimes \pi) + \varepsilon \text{KL}(\pi|\mu \otimes \nu), \quad (\text{QEOT})$$

where $Q_{c_{\mathcal{X}}, c_{\mathcal{Y}}}(\mathbf{x}, \mathbf{y}, \mathbf{x}', \mathbf{y}') := |c_{\mathcal{X}}(\mathbf{x}, \mathbf{x}') - c_{\mathcal{Y}}(\mathbf{y}, \mathbf{y}')|^2$ measures the pointwise cost distortion. With $\varepsilon = 0$, we recover the Gromov-Wasserstein (Mémoli, 2011) problem. This is the standard OT formulation for measures supported on *incomparable* spaces. Using $\varepsilon > 0$ offers computational advantages, since for discrete μ, ν , we can solve (QEOT) with a mirror-descent scheme iterating the Sinkhorn algorithm (Peyré et al., 2016). This solver has $\mathcal{O}(n^2)$ or $\mathcal{O}(n^3)$ time complexity, depending on $c_{\mathcal{X}}$ and $c_{\mathcal{Y}}$ (Scetbon et al., 2022, Alg. 1 & Alg. 2), and $\mathcal{O}(n^2)$ memory complexity.

Unbalanced Extensions. The EOT formulations presented above can only handle measures with the same total mass. Unbalanced optimal transport (UOT) (Liero et al., 2018; Chizat et al., 2018) lifts this constraint by penalizing the deviation of $p_1 \# \pi$ to μ and $p_2 \# \pi$ to ν with a divergence. Using the KL and introducing weightings $\lambda_1, \lambda_2 > 0$ the unbalanced extension of (LEOT) reads

$$\min_{\pi \in \mathcal{M}^+(\mathcal{X} \times \mathcal{Y})} \int_{\mathcal{X} \times \mathcal{Y}} c d\pi + \varepsilon \text{KL}(\pi|\mu \otimes \nu) + \lambda_1 \text{KL}(\pi_1|\mu) + \lambda_2 \text{KL}(\pi_2|\nu). \quad (\text{ULEOT})$$

This problem can be solved efficiently in the discrete setting using a variant of the Sinkhorn algorithm (Frogner et al., 2015; Séjourné et al., 2023a). Analogously, quadratic OT also admits an unbalanced generalization, which reads

$$\min_{\pi \in \mathcal{M}^+(\mathcal{X} \times \mathcal{Y})} \int_{(\mathcal{X} \times \mathcal{Y})^2} Q_{c_{\mathcal{X}}, c_{\mathcal{Y}}} d(\pi \otimes \pi) + \varepsilon \text{KL}^{\otimes}(\pi|\mu \otimes \nu) + \lambda_1 \text{KL}^{\otimes}(\pi_1|\mu) + \lambda_2 \text{KL}^{\otimes}(\pi_2|\nu), \quad (\text{UQEOT})$$

where $\text{KL}^\otimes(\rho|\gamma) = \text{KL}(\rho \otimes \rho | \gamma \otimes \gamma)$. This can be solved using an extension of Peyré et al. (2016)’s scheme introduced by Séjourné et al. (2023b). Each solver has the same time and memory complexity as its balanced counterpart. For both (ULEOT) and (UQEOT), instead of selecting λ_i , we introduce $\tau_i = \frac{\lambda_i}{\lambda_i + \varepsilon}$ s.t. we recover the hard marginal constraint for $\tau_i = 1$, when $\lambda_i \rightarrow +\infty$. We write $\tau = (\tau_1, \tau_2)$.

Flow Matching. Given a prior $\rho_0 \in \mathcal{M}_1^+(\mathbb{R}^d)$ and a time-dependent vector field $(v_t)_{t \in [0,1]}$, one can define a probability path p_t starting from ρ_0 using the flow ϕ_t solving

$$\frac{d}{dt} \phi_t(\mathbf{z}) = v_t(\phi_t(\mathbf{z})), \quad \phi_0(\mathbf{z}) = \mathbf{z}, \quad (1)$$

by setting $p_t = \phi_t \# \rho_0$. We then say that v_t generates the path p_t . Continuous Normalizing Flows (Chen et al., 2018) (CNFs) model $v_{t,\theta}$ with a neural network, which is trained to match a terminal condition $p_1 = \rho_1 \in \mathcal{M}_1^+(\mathbb{R}^d)$. Conditional Flow Matching (CFM) (Lipman et al., 2023) is a simulation-free technique to train CNFs by constructing individual paths between samples, and minimizing

$$\mathbb{E}_{t, Z_0 \sim \rho_0, Z_1 \sim \rho_1} [\|v_{t,\theta}([Z_0, Z_1]_t) - (Z_1 - Z_0)\|_2^2], \quad (2)$$

where $[Z_0, Z_1]_t := (1-t)Z_0 + tZ_1$ with $t \sim \mathcal{U}([0,1])$. If this loss is 0, the flow maps ρ_0 to ρ_1 , i.e., $\phi_1 \# \rho_0 = \rho_1$.

3. Generative Entropic Neural OT

In this section, we introduce GENOT, a method to learn EOT couplings by learning their conditional distributions. In § 3.1, we focus on balanced OT, and show that GENOT approximates linear or quadratic EOT couplings, solutions to (LEOT) or (QEOT) respectively. Second, in § 3.2, we extend GENOT to the unbalanced setting by loosening the conservation of mass constraint. We define U-GENOT, which approximates solutions to (ULEOT) and (UQEOT). Finally, in § 3.3, we highlight that GENOT also addresses a fused problem, combining (LEOT) and (QEOT).

3.1. Learning Entropic Couplings with GENOT

Let $\mu \in \mathcal{M}_1^+(\mathcal{X})$, $\nu \in \mathcal{M}_1^+(\mathcal{Y})$ and π_ε^* be an EOT coupling between μ and ν , which can be a solution of problem (LEOT) or (QEOT). By the measure disintegration theorem:

$$d\pi_\varepsilon^*(\mathbf{x}, \mathbf{y}) = d\mu(\mathbf{x}) d\pi_\varepsilon^*(\mathbf{y}|\mathbf{x}).$$

Knowing μ , we can hence fully describe π_ε^* via the conditional distributions $(\pi_\varepsilon^*(\cdot|\mathbf{x}))_{\mathbf{x} \in \mathcal{X}}$. The latter are also of great practical interest, as they provide a way to transport a point \mathbf{x} sampled from μ to the target domain \mathcal{Y} ; either *stochastically* by sampling $\mathbf{y}_1, \dots, \mathbf{y}_n$ from $\pi_\varepsilon^*(\cdot|\mathbf{x})$, or *deterministically* by averaging over conditional samples: $T_\varepsilon(\mathbf{x}) := \mathbb{E}_{Y \sim \pi_\varepsilon^*(\cdot|\mathbf{x})}[Y]$. Moreover, we can assess the uncertainty of these predictions using any statistic of $\pi_\varepsilon^*(\cdot|\mathbf{x})$.

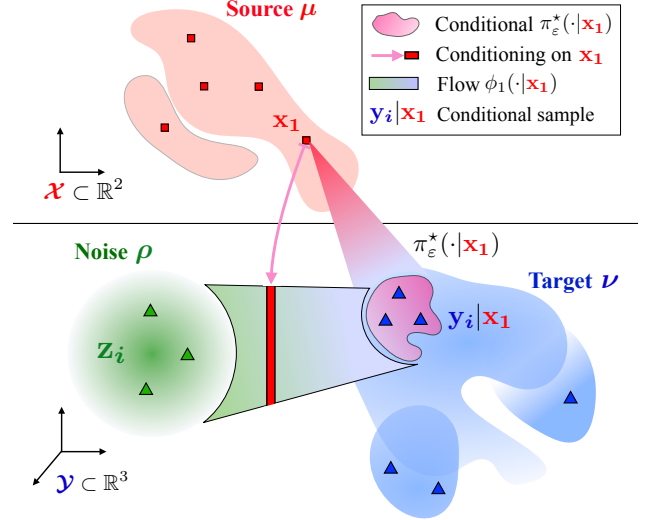


Figure 1. Sketch of the GENOT model. For each \mathbf{x} in the support of the source μ , we learn a flow $\phi_1(\cdot|\mathbf{x})$ from the noise ρ to the conditional $\pi_\varepsilon^*(\cdot|\mathbf{x})$, whose support lies in that of the target ν . We highlight this procedure for a specific point \mathbf{x}_1 .

This aspect is crucial for many real-world problems, especially in single-cell biology, as shown in section 5.1.

Learning the Conditional Distributions. Let $\rho = \mathcal{N}(0, I_q)$ the standard Gaussian on the target space $\mathbb{R}^q \supset \mathcal{Y}$. From the noise outsourcing lemma (Kallenberg, 2002), there exists a collection of conditional generators $\{T^*(\cdot|\mathbf{x})\}_{\mathbf{x} \in \mathcal{X}}$ s.t. $T^*(\cdot|\mathbf{x}) : \mathbb{R}^q \rightarrow \mathbb{R}^q$ and for each \mathbf{x} in the support of μ , $\pi_\varepsilon^*(\cdot|\mathbf{x}) = T^*(\cdot|\mathbf{x}) \# \rho$. This means that if $Z \sim \rho$, then $Y = T^*(Z|\mathbf{x}) \sim \pi_\varepsilon^*(\cdot|\mathbf{x})$. Here, we seek to learn a neural collection $\{T_\theta(\cdot|\mathbf{x})\}_{\mathbf{x} \in \mathcal{X}}$ of such conditional generators, fitting the constraint $T_\theta(\cdot|\mathbf{x}) \# \rho = \pi_\varepsilon^*(\cdot|\mathbf{x})$, for any \mathbf{x} in the support of μ . We employ the CFM framework (see § 2) and parameterize each $T_\theta(\cdot|\mathbf{x})$ implicitly, as the flow induced by a neural vector field $v_{t,\theta}(\cdot|\mathbf{x}) : \mathbb{R}^q \rightarrow \mathbb{R}^q$. Namely, $T_\theta(\cdot|\mathbf{x}) = \phi_1(\cdot|\mathbf{x}) : \mathbb{R}^q \rightarrow \mathbb{R}^q$ where $\phi_t(\cdot|\mathbf{x})$ solves

$$\frac{d}{dt} \phi_t(\mathbf{z}|\mathbf{x}) = v_{t,\theta}(\phi_t(\mathbf{z}|\mathbf{x})|\mathbf{x}), \quad \phi_0(\mathbf{z}|\mathbf{x}) = \mathbf{z}. \quad (3)$$

We stress that while $\mathbf{x} \in \mathcal{X} \subset \mathbb{R}^d$, the flow $\phi_1(\cdot|\mathbf{x})$ from ρ to $\pi_\varepsilon^*(\cdot|\mathbf{x})$ is defined on the target space $\mathbb{R}^q \supset \mathcal{Y}$. Hence, we can map samples *within* the same space when $p = q$, but also *across* incomparable spaces when $p \neq q$. In particular, this allows us to consider the quadratic OT problem (QEOT). Thus, for each \mathbf{x} , we optimize $v_{t,\theta}(\cdot|\mathbf{x})$ by minimizing the CFM loss (2) to map ρ to $\pi_\varepsilon^*(\cdot|\mathbf{x})$, i.e.

$$\mathbb{E}_{t, Z \sim \rho, Y \sim \pi_\varepsilon^*(\cdot|\mathbf{x})} [\|v_{t,\theta}([Z, Y]_t|\mathbf{x}) - (Y - Z)\|_2^2]. \quad (4)$$

where $[Z, Y]_t = (1-t)Z + tY$ interpolates between noise and conditional vectors. Averaging for all \mathbf{x} in the support of μ and using Fubini’s Theorem, we derive $\mathcal{L}_{\text{GENOT}}(\theta)$:

$$\mathbb{E}_{t, Z \sim \rho, (X, Y) \sim \pi_\varepsilon^*} [\|v_{t,\theta}([Y, Z]_t|X) - (Y - Z)\|_2^2]. \quad (5)$$

In practice, we optimize a *sample-based* GENOT loss by estimating $\pi_\varepsilon^n = \sum_{i,j} \mathbf{P}_\varepsilon^{ij} \delta_{(X_i, Y_j)}$, from $X_1, \dots, X_n \sim \mu$ and $Y_1, \dots, Y_n \sim \nu$, with a *discrete* EOT solver, see Alg. 1.

GENOT Preserves the Coupling Information, in the sense that, in the infinite sample regime, one could provably recover the original entropic coupling, whether in the linear or quadratic OT settings, and for any cost function.

Proposition 3.1 (Well-posedness of GENOT.). *Suppose that $\mathcal{L}_{\text{GENOT}}(\theta) = 0$. Then, for $X \sim \mu$, $Z \sim \rho$ and $Y = \phi_1(Z|X)$ denoting the solution of ODE (3), one has $Y \sim \pi_\varepsilon^*(\cdot|X)$, and hence $(X, Y) \sim \pi_\varepsilon^*$.*

This result is noteworthy since standard flow matching only preserves straight couplings (Liu et al., 2022), while bridge matching (its stochastic counterpart) only preserves the linear EOT coupling for $c(\mathbf{x}, \mathbf{y}) = \|\mathbf{x} - \mathbf{y}\|_2^2$, as shown recently by Bortoli et al. (2023). In contrast, GENOT is a conditional CFM model, learning the conditional distributions of the coupling independently of each other: For each \mathbf{x} , we leverage CFM to learn a conditional flow $\phi_1(\cdot|\mathbf{x})$ that maps ρ to $\pi_\varepsilon^*(\cdot|\mathbf{x})$. In this sense, GENOT can be conceptualized as an *augmented flow matching* procedure. We visualize that GENOT preserves the coupling information in Fig. 2.

GENOT Handles Any Cost. As GENOT preserves the coupling information, we can use it to approximate linear or quadratic EOT couplings. In both cases, we make no assumptions on the cost functions: We only need to evaluate them on samples to estimate π_ε^* using a discrete solver, see GENOT Alg. 1, line 5. In particular, we can use implicitly defined costs, whose evaluation requires a non-differentiable sub-routine. For instance, we can use the geodesic distance on the data manifold, which can be approximated from the shortest path distance on the k -nn graph induced by the Euclidean distance (Crane et al., 2013; Solomon et al., 2015). Using such a data-driven cost function in discrete OT pipelines has demonstrated its effectiveness in a range of single-cell genomics tasks (Demetci et al., 2022; Huguet et al., 2022; Klein et al., 2023), as comparing cells using ℓ_p distances often fails to capture discrepancies in gene expression space (Moon et al., 2018). With GENOT, we extend the use of this cost to the neural setting, for both linear (see § 5.1) and quadratic OT (see § 5.2).

GENOT Approximates Conditional Densities. For each \mathbf{x} , we build a CNF $p_t(\cdot|\mathbf{x}) = \phi_t(\cdot|\mathbf{x})\#_t \rho$ between $p_0 = \rho$ and $p_1 = \pi_\varepsilon^*(\cdot|\mathbf{x})$. From the instantaneous change of variables formula (Chen et al., 2018), we can then approximate the conditional density $\pi_\varepsilon^*(\mathbf{y}|\mathbf{x})$ at an arbitrary point $\mathbf{y} \in \mathcal{Y}$. We use it, for instance, in Figures 3, 6, 17 and 21.

3.2. U-GENOT: Extension to the Unbalanced Setting

Re-Balancing the UOT Problems. In its standard form, GENOT respects marginal constraints, so it cannot directly

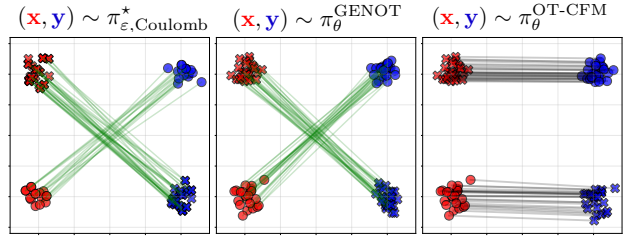


Figure 2. Fitting the EOT coupling between two Gaussian mixtures for the Coulomb cost (Benamou et al., 2015) $c(\mathbf{x}, \mathbf{y}) = 1/\|\mathbf{x} - \mathbf{y}\|_2$, and $\varepsilon = 0.01$, using GENOT and OT-CFM (Tong et al., 2023b). We connect paired samples with a line. The EOT coupling pairs **source** samples and **target** samples diagonally (left). GENOT (middle) **generates samples** correctly, while OT-CFM (right) fails to preserve the information from mini-batch couplings. The data-setting is inspired by Bortoli et al. (2023, Fig. 1)

handle unbalanced formulations (ULEOT) or (UQEOT). We show that unbalanced EOT problems can be *re-balanced*. Eyring et al. (2023); Lübeck et al. (2022); Yang & Uhler (2019) introduced previously these ideas in the Monge map estimation setting, namely, in a static and deterministic setup. Our method stems from the fact that, for both linear and quadratic OT, the unbalanced EOT coupling $\pi_{\varepsilon, \tau}^*$ between $\mu \in \mathcal{M}^+(\mathcal{X})$ and $\nu \in \mathcal{M}^+(\mathcal{Y})$ solves a balanced EOT problem between its marginals, which are re-weighted versions $\tilde{\mu}$ and $\tilde{\nu}$ of μ and ν , that have the same mass.

Proposition 3.2 (Re-Balancing the unbalanced problems.). *Let $\pi_{\varepsilon, \tau}^*$ be an unbalanced EOT coupling, solution of (ULEOT) or (UQEOT) between $\mu \in \mathcal{M}^+(\mathcal{X})$ and $\nu \in \mathcal{M}^+(\mathcal{Y})$. We note $\tilde{\mu} = p_1\#_t \pi_{\varepsilon, \tau}^*$ and $\tilde{\nu} = p_2\#_t \pi_{\varepsilon, \tau}^*$ its marginals. Then, in both cases, $\tilde{\mu}$ (resp. $\tilde{\nu}$) has a density w.r.t μ (resp. ν) i.e. it exists $\eta, \xi : \mathbb{R}^d \rightarrow \mathbb{R}^+$ s.t. $\tilde{\mu} = \eta \cdot \mu$ and $\tilde{\nu} = \xi \cdot \nu$. Moreover, $\tilde{\mu}$ and $\tilde{\nu}$ have the same mass*

1. (Linear) $\pi_{\varepsilon, \tau}^*$ solves the balanced problem (LEOT) between $\tilde{\mu}$ and $\tilde{\nu}$ with the same ε .
2. (Quadratic) Provided that $c_{\mathcal{X}}$ and $c_{\mathcal{Y}}$ (or $-c_{\mathcal{X}}$ and $-c_{\mathcal{Y}}$) are conditionally positive kernels (see Def. A.1), $\pi_{\varepsilon, \tau}^*$ solves the balanced problem (QEOT) between $\tilde{\mu}$ and $\tilde{\nu}$ with $\varepsilon' = m(\pi_{\varepsilon, \tau}^*) \varepsilon$, where $m(\pi_{\varepsilon, \tau}^*) = \pi_{\varepsilon, \tau}^*(\mathcal{X} \times \mathcal{Y})$.

Learning the Coupling and the Re-Weightings Simultaneously. Thanks to Prop. 3.2, we aim to [i] learn a balanced EOT coupling between $\tilde{\mu}$ and $\tilde{\nu}$ along with [ii] the re-weighting functions η, ξ . Learning them is desirable since they model the creation and destruction of mass. We do both simultaneously by adapting the GENOT procedure. More formally, we seek to optimize $\mathcal{L}_{\text{U-GENOT}}(\theta)$:

$$\begin{aligned} & \mathbb{E}_{t, Z \sim \rho, (X, Y) \sim \pi_{\varepsilon, \tau}^*} [\|v_{t, \theta}([Z, Y]_t | X) - (Y - Z)\|_2^2] \quad \text{[i]} \\ & + \mathbb{E}_{X \sim \mu} [(\eta - \eta_\theta)(X)^2] + \mathbb{E}_{Y \sim \nu} [(\xi - \xi_\theta)(Y)^2] \quad \text{[ii]} \end{aligned}$$

As with GENOT, we simply need to estimate a discrete unbalanced EOT coupling $\pi_{\varepsilon, \tau}^n$ from samples to estimate

that loss. We build upon theoretical insights on the linear OT case and extend them to the quadratic OT case in practice.

Proposition 3.3 (Pointwise estimation of re-weighting functions.). *Let $\pi_{\varepsilon,\tau}^n = \sum_{i,j} \mathbf{P}_{\varepsilon,\tau}^{i,j} \delta_{(X_i, Y_j)}$, solution to (ULEOT) between empirical counterparts of μ and ν . Let $\mathbf{a} = \mathbf{P}_{\varepsilon,\tau} \mathbf{1}_n$ and $\mathbf{b} = \mathbf{P}_{\varepsilon,\tau}^\top \mathbf{1}_n$ its marginals weights. Then, almost surely, $n a_i \rightarrow \eta(X_i)$ and $n b_i \rightarrow \xi(Y_i)$.*

Using Prop. 3.2, $\hat{\pi}_{\varepsilon,\tau}^n$ is a balanced EOT coupling between its marginals, which are empirical approximations of $\tilde{\mu}$ and $\tilde{\nu}$. Hence, we estimate the term [i] of the loss as we do in the balanced case by sampling from the discrete coupling. Furthermore, Prop.3.3 highlights that the estimation of $\hat{\pi}_{\varepsilon,\tau}^n$ also provides a consistent estimate of the re-weighting function evaluations at each X_i and Y_i . This enables estimating [ii]. Therefore, switching from GENOT to U-GENOT simply involves using an unbalanced solver instead of a balanced one, and regressing the re-weightings on the marginal weights of the estimated discrete coupling. We detail our procedure in Alg. 1, showing the additional steps w.r.t. GENOT in teal.

3.3. Combining Linear and Quadratic OT

We show in § 3.1 and § 3.2 how to use GENOT to solve OT problems within the same space or across incomparable spaces. On the other hand, numerous real-world problems pose the challenge of the source and target domains being only *partially* incomparable (Vayer et al., 2018). Therefore, suppose that the source and target space can be decomposed as $\mathcal{X} = \Omega \times \mathcal{X}'$ and $\mathcal{Y} = \Omega \times \mathcal{Y}'$, respectively. Intuitively, a sample $(\mathbf{u}, \mathbf{x}) \in \Omega \times \mathcal{X}'$ can be interpreted as a structural information \mathbf{x} equipped with a feature \mathbf{u} . Afterwards, assume we are given a cost $c : \Omega \times \Omega \rightarrow \mathbb{R}$ to compare features, along with the intra-domain costs $c_{\mathcal{X}'}, c_{\mathcal{Y}'}$. The entropic Fused Gromov-Wasserstein (FGW) problem reads

$$\min_{\pi \in \Pi(\mu, \nu)} \int_{(\mathcal{X} \times \mathcal{Y})^2} Q_{c_{\mathcal{X}'}, c_{\mathcal{Y}'}}^c d(\pi \otimes \pi) + \varepsilon \text{KL}(\pi | \mu \otimes \nu),$$

EFGW

where $Q_{c_{\mathcal{X}'}, c_{\mathcal{Y}'}}^c((\mathbf{u}, \mathbf{x}), (\mathbf{v}, \mathbf{y}), \mathbf{x}', \mathbf{y}') := (1 - \alpha) c(\mathbf{u}, \mathbf{v}) + \alpha |c_{\mathcal{X}'}(\mathbf{x}, \mathbf{x}') - c_{\mathcal{Y}'}(\mathbf{y}, \mathbf{y}')|^2$ and $\alpha \in [0, 1]$. This loss combines the pointwise structural distortion and the feature information. The fused problem (EFGW) also admits an unbalanced extension, which can be derived in the same way as (UQEOT) using the quadratic KL^\otimes (Thual et al., 2023).

(U-)GENOT for the Fused Setting. Whether in the balanced or unbalanced setting, we can use our method to learn a specific coupling as soon as it can be estimated from samples. We stress that the discrete solvers we use for (QEOT) and (UQEOT), respectively Peyré et al. (2016)’s and Séjourné et al. (2023b)’s ones, are still applicable in the fused setting. As a result, we can approximate solutions of (EFGW) and its unbalanced counterpart with (U-)GENOT. To illustrate the learning outcome, take a solution

Algorithm 1 U-GENOT. Skip teal steps for GENOT.

- 1: **Require parameters:** Batch size n ; entropic regularization ε ; **unbalancedness parameter** τ ; *linear, quadratic or fused* discrete OT solver $\text{Solver}_{\varepsilon,\tau}$.
- 2: **Require network:** Time-dependent conditional velocity field $v_{t,\theta}(\cdot|\cdot) : \mathbb{R}^q \times \mathbb{R}^p \rightarrow \mathbb{R}^q$; **re-weighting functions** $\eta_\theta : \mathbb{R}^p \rightarrow \mathbb{R}, \xi_\theta : \mathbb{R}^q \rightarrow \mathbb{R}$.
- 3: **for** $t = 1, \dots, T_{\text{iter}}$ **do**
- 4: Sample $X_1, \dots, X_n \sim \mu$ and $Y_1, \dots, Y_n \sim \nu$.
- 5: $\mathbf{P}_{\varepsilon,\tau} \leftarrow \text{Solver}_{\varepsilon,\tau}(\{X_i\}_{i=1}^n, \{Y_j\}_{j=1}^n) \in \mathbb{R}_+^{n \times n}$.
- 6: $\mathbf{a} \leftarrow \mathbf{P}_{\varepsilon,\tau} \mathbf{1}_n$ and $\mathbf{b} \leftarrow \mathbf{P}_{\varepsilon,\tau}^\top \mathbf{1}_n$.
- 7: Sample $(i_1, j_1), \dots, (i_n, j_n) \sim \mathbf{P}_{\varepsilon,\tau}$.
- 8: Sample $Z_1, \dots, Z_n \sim \rho$ and $t_1, \dots, t_n \sim \mathcal{U}([0, 1])$.
- 9: $\mathcal{L}(\theta) \leftarrow \sum_k \|v_{t_k, \theta}([Z_k, Y_{j_k}] | X_{i_k}) - (Y_{j_k} - Z_k)\|_2^2$
- 10: $\quad + \sum_k (\eta_\theta(X_k) - n \mathbf{a}_k)^2 + (\xi_\theta(Y_k) - n \mathbf{b}_k)^2$.
- 11: $\theta \leftarrow \text{Update}(\theta, \frac{1}{n} \nabla \mathcal{L}(\theta))$.
- 12: **end for**

π_α^* of (EFGW). Learning π_α^* with our method amounts to training vector fields that are conditioned on pairs of modalities from the source domain $v_{t,\theta}(\cdot | \mathbf{u}, \mathbf{x})$, to sample pairs of modalities from the target domain via the flow: $Z \sim \rho, \phi_1(Z | \mathbf{u}, \mathbf{x}) = (V, Y) \sim \pi_\alpha^*(\cdot | \mathbf{u}, \mathbf{x})$. The sampled modalities (V, Y) (i) minimize transport cost quantified by c along the feature (ii) while minimizing the distortion along the structural information quantified by $c_{\mathcal{X}'}$ and $c_{\mathcal{Y}'}$. In § 5.2, we use fused couplings to enhance the translation between different modalities of cells by adding label information .

4. Related work and Discussions

Static Neural EOT. While GENOT is the first model to consider the quadratic (and Fused) EOT setting, as well as addressing unbalancedness, various methods have been proposed in the (balanced) linear EOT scenario. The first class of methods solves (LEOT) dual. While some of them (Seguy et al., 2017; Genevay et al., 2019a) do not allow direct sampling from to π_ε^* , Daniels et al. (2021) and Mokrov et al. (2023) model the conditional distributions $\pi_\varepsilon^*(\cdot | \mathbf{x})$. However, these methods might be costly and unstable, as they rely on Langevin sampling during training or inference.

Dynamic Neural EOT. The second class of linear EOT solvers builds upon the link between (LEOT) and the SB problem (De Bortoli et al., 2021; Chen et al., 2021; Vargas et al., 2021; Gushchin et al., 2022). As simulations are costly in this setting, recent works consider simulation-free training via bridge matching (Shi et al., 2023; Korotin et al., 2023a; Liu et al., 2023; Zhou et al., 2023; Peluchetti, 2023; Tong et al., 2023a;b). While Tong et al. (2023a;b), use mini-batch OT similarly to us, our method is fundamentally different, as we do not build upon the link between EOT and SB. We only use flow matching as a powerful black box

to learn a flow from the noise ρ to each conditional $\pi_\varepsilon^*(\cdot|\mathbf{x})$. Therefore, our approach allows for more flexibility. First (i), the abovementioned methods assume that $\mathcal{X}, \mathcal{Y} \subset \mathbb{R}^d$, since they learn a velocity field (or a drift) by directly bridging $\mathbf{x} \in \mathcal{X}, \mathbf{y} \in \mathcal{Y}$. Then, they map μ to ν with the induced (stochastic) flow. On the other hand, conditionally to each $\mathbf{x} \in \mathcal{X} \subset \mathbb{R}^d$, we learn a velocity field $v_{t,\theta}(\cdot|\mathbf{x}) : \mathbb{R}^q \rightarrow \mathbb{R}^q$ in the *target space*, by building paths between noise $\mathbf{z} \in \mathbb{R}^q$ and $\mathbf{y} \in \mathcal{Y} \subset \mathbb{R}^q$. Then, we map ρ to each $\pi_\varepsilon^*(\cdot|\mathbf{x})$ with the flows $\phi_1(\cdot|\mathbf{x})$, and recover $\nu = \phi_1(\cdot|\cdot)\#(\rho \otimes \mu)$. Second (ii), since they use discrete couplings to pair the samples \mathbf{x}, \mathbf{y} that they bridge, they can only approximate the SB for $c(\mathbf{x}, \mathbf{y}) = \|\mathbf{x} - \mathbf{y}\|_2^2$. This results from (Bortoli et al., 2023, Prop. 2). In contrast, our method handles any cost, as shown in Fig 2. Third (iii), as they learn a single flow directly transporting μ to ν , they do not approximate the conditional densities $\pi_\varepsilon^*(\mathbf{y}|\mathbf{x})$. Similarly to Tong et al. (2023b), Pooladian et al. (2023) couple samples from μ and ν , but they only model deterministic maps and assume $\mu = \mathcal{N}(0, I_d)$. Finally, Bortoli et al. (2023) have recently proposed an augmented bridge matching procedure that preserves couplings. Yet, they still require $\mathcal{X}, \mathcal{Y} \subset \mathbb{R}^d$ and do not approximate conditional densities.

Mini-batches and Biases Quantifying non-asymptotically the bias resulting from minimizing a sample-based GENOT loss, and *not* its population value, is challenging. The OT curse of dimensionality (Weed & Bach, 2017) has been discussed in generative models relying on mini-batch couplings (Genevay et al., 2019a; Fatras et al., 2021; Tong et al., 2023b;a). Yet, our goal is *not* to model *non-regularized* OT, such as a deterministic Monge map, or a Benamou-Brenier vector field. We explicitly target the *entropy-regularized* OT coupling. Thus, using $\varepsilon \gg 0$ helps to mitigate the curse of dimensionality because of two qualitative factors:

- (i) **Statistical.** For both linear and quadratic OT, all statistical recovery rates that relate to entropic costs (Genevay et al., 2019b; Zhang et al., 2023) or maps (Pooladian & Niles-Weed, 2021; Rigollet & Stromme, 2022), have a far more favorable regime, with a parametric rate in $\varepsilon > 0$ that dodges the curse of dimensionality.
- (ii) **Computational.** While the benefits of employing a large enough ε in Sinkhorn’s algorithm are widely known, Rioux et al. (2023) have recently shown that as ε increases, the quadratic OT problem (QEOT) becomes convex, making discrete solvers faster and more reliable.

To demonstrate this aspect, we empirically study the influence of the batch size on GENOT, using data from a recent benchmark (Gushchin et al., 2023), see Fig. 9.

5. Experiments

We show the applicability and versatility of our framework to map within the same space (solving a linear EOT prob-

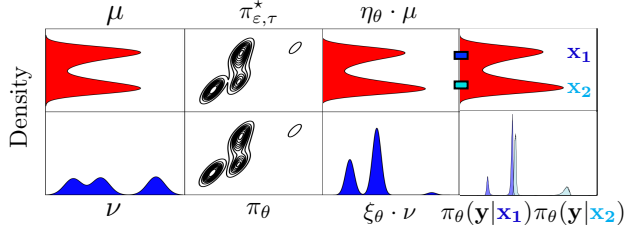


Figure 3. Estimating the (ULEOT) coupling between Gaussian mixtures with U-GENOT-L ($\varepsilon = 0.05$, $\tau_1 = \tau_2 = 0.98$ and $c = \ell_2^2$). Left to right: Source (top) μ and the target ν (bottom), learned (top) and true (bottom) coupling, learned (top) and true (bottom) re-weighted marginal, and conditional densities. We further showcase the influence of τ_1, τ_2 in Fig. 11.

Model	rank $\text{BW}_2^2\text{-UVP}$	rank $\text{cBW}_2^2\text{-UVP} \downarrow$
LSOT	9.33	9.33
SCONES	7.50	7.67
DiffSB	7.58	7.50
FB-SDE-J	5.12	7.33
FB-SDE-A	6.75	6.75
EgNOT	2.71	5.75
ENOT	6.08	3.00
NOT	4.92	2.92
MLE-SB	3.17	2.67
GENOT-L	1.79	2.08

Table 1. Average ranks of each method across experiments, on estimating the ground-truth EOT coupling π_ε^* between each pair of measures μ, ν , in dimension $d \in \{2, 16, 64, 128\}$ and $\varepsilon \in \{0.1, 1, 10\}$ of Gushchin et al. (2023)’s benchmark. As them, we measure performances with both $\text{BW}_2^2\text{-UVP}$ (34) and $\text{cBW}_2^2\text{-UVP}$ (36) metrics. See App. E.1 for details.

lem) and across incomparable spaces (solving a purely quadratic or fused EOT problem). Metrics and datasets are discussed in App. B and App. C, respectively. Further experimental details or results are reported in App. D. Setups for baselines are listed in App. E. Implementation details can be found in App. F. We denote by **GENOT-L** the GENOT model for solving the linear problem (LEOT), **GENOT-Q** for the quadratic (QEOT) and **GENOT-F** for the fused (EFGW) one. When considering the **unbalanced** counterparts, we add the **prefix U**. Moreover, when using the **conditional mean** of a GENOT model, we add the **suffix CM**. We denote our estimated couplings by π_θ .

5.1. GENOT for Linear EOT problems

GENOT-L on a static SB benchmark. First, we show that GENOT accurately computes EOT couplings using a recent benchmark. For different $\varepsilon \in \{0.1, 1, 10\}$ and $d \in \{2, 16, 64, 128\}$, Gushchin et al. (2023) consider pairs μ, ν for which the π_ε^* solution of (LEOT) with ℓ_2^2 cost $c(\mathbf{x}, \mathbf{y}) = \frac{1}{2} \|\mathbf{x} - \mathbf{y}\|_2^2$ is known. Tab. 1 shows that GENOT-L outperforms *all* baselines, choosing *one configuration*

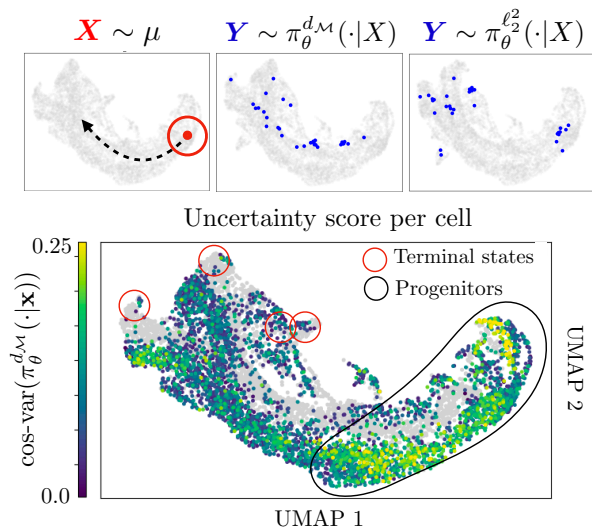


Figure 4. **Top:** Source cell from the early time points (top left) and samples of the conditional distributions of the EOT coupling learned with GENOT for the geodesic cost $d_{\mathcal{M}}$ (middle) and the ℓ_2^2 cost (right) projected onto a UMAP (McInnes et al., 2018). Using the geodesic distance as cost function prevents π_{θ} from skipping the intermediate cell population, which is far away from the source cell and terminal cells in ℓ_2 distance. **Bottom:** UMAP colored according to the uncertainty score $\text{cos-var}(\pi_{\theta}^{d_{\mathcal{M}}}(\cdot|X))$ of each source cell \mathbf{x} . Target cells are colored in gray.

for all experiments as opposed to some baselines. Detailed results can be found in Tab. 2 and 3. Importantly, GENOT’s performance can be further improved when adapting the batch size, see Fig. 9. These results are of particular significance since many baselines are tailored towards the specific task of solving (i) the linear EOT problem (LEOT), (ii) in the balanced setting (iii) with the ℓ_2^2 cost. In contrast, the contributions of GENOT go beyond this restrictive setting. In the following, we demonstrate GENOT’s flexibility and highlight its relevance in various single-cell biology tasks.

U-GENOT-L on simulated data. To go beyond the balanced setting, Fig. 3 visualizes U-GENOT-L’s ability to learn unbalanced EOT plans and re-weighting functions. We further showcase the influence of τ_1, τ_2 in Fig. 11.

GENOT-L recovers single cell trajectories. We demonstrate GENOT-L’s capability to infer the development of cells on a dataset capturing gene expression of the developing mouse pancreas at embryonic days 14.5 (source) and 15.5 (target) (Bastidas-Ponce et al., 2019). As cells are known to evolve stochastically (Elowitz et al., 2002), we leverage GENOT’s capability to generate samples from the conditional distribution to model non-deterministic trajectories. Moreover, as Euclidean metrics often fail to represent meaningful distances in gene expression space (Moon et al., 2018), we leverage GENOT’s flexibility and use the geodesic distance on the data manifold $d_{\mathcal{M}}$ as cost, as discussed in § 3.1. Here, $\mathcal{M} = \mathcal{X} \cup \mathcal{Y}$ since the source and

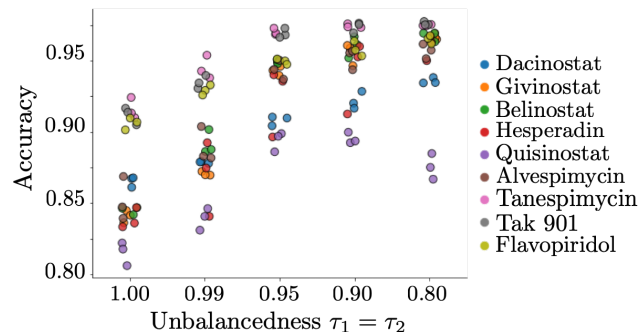


Figure 5. Accuracy of cellular response predictions of U-GENOT-L for different cancer drugs with varying unbalancedness parameter $\tau = \tau_1 = \tau_2$. As τ decreases, we allow for more unbalancedness. For each τ , we display results on 3 runs.

target domains have the same dimension. We also estimate the EOT coupling for the ℓ_2^2 cost for comparison. Fig. 4 and Fig. 13 highlight that the geodesic cost causes the conditional distribution to follow the data manifold. In particular, this helps to obtain biologically more plausible cell trajectories. We follow Gayoso et al. (2022) for assessing the uncertainty of cell trajectories by computing $\text{cos-var}(\pi_{\theta}(\cdot|\mathbf{x})) = \text{Var}_{Y \sim \pi_{\theta}(\cdot|\mathbf{x})}[\text{cos-sim}(Y, \mathbb{E}_{Y \sim \pi_{\theta}(\cdot|\mathbf{x})}[Y])]$. See App. B.1 for more details on cos-var . We expect high uncertainty in cell types in early developmental stages and low variance in mature cell types. Indeed, Fig. 4 and Fig. 12 show that the computed uncertainty is biologically meaningful: GENOT-L helps to uncover lineage branching events.

U-GENOT-L predicts single-cell responses to perturbations. Neural OT has been successfully applied to model cellular responses to perturbations using deterministic maps (Bunne et al., 2021). GENOT has the comparative advantage to model conditional distributions, allowing for uncertainty quantification. We consider single cell RNA-seq data measuring the response of cells to 163 cancer drugs (Srivatsan et al., 2020). Each drug has been applied to a population of cells that can be partitioned into 3 different cell types. Source (resp. target) is cells before (resp. after) drug application. While there is no ground truth in the matching between unperturbed and perturbed cells due to the destructive nature of sequencing technologies, we know which unperturbed subset of cells is supposed to be mapped to which perturbed subset of cells. We use this to define an accuracy metric (see App. B.2), while we assess the uncertainty of the prediction using cos-var . Fig. 14 shows that for 117 out of 163 drugs, the model is perfectly calibrated (see App. B.1), while it yields a negative correlation between error and uncertainty only for one drug. We can improve predictions by accounting for class imbalances between different cell types using U-GENOT. Indeed, Fig. 5.1 shows that allowing for mass variation increases accuracy for nine different cancer drugs, which we selected as they are known to have a strong effect. Fig. 15 and 16 confirm the results visually.

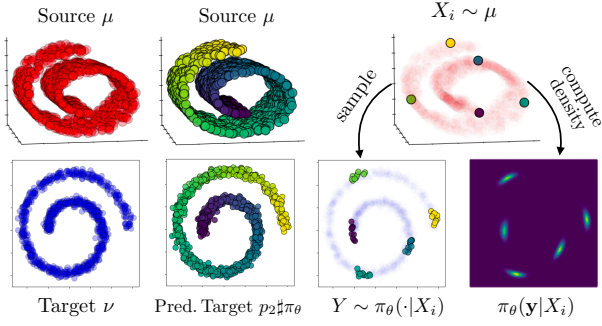


Figure 6. Mapping a Swiss roll in \mathbb{R}^3 (μ , top left) to a spiral in \mathbb{R}^2 (ν , bottom left) with GENOT-Q. Center: Color code tracks where samples from μ (top) are mapped to (bottom). Right column: samples from μ (top) and each of the corresponding conditionals, along with conditional density estimates. The learned QEOT coupling minimizes the cost distortion: Points close in support of μ are paired to points close in the support of ν .

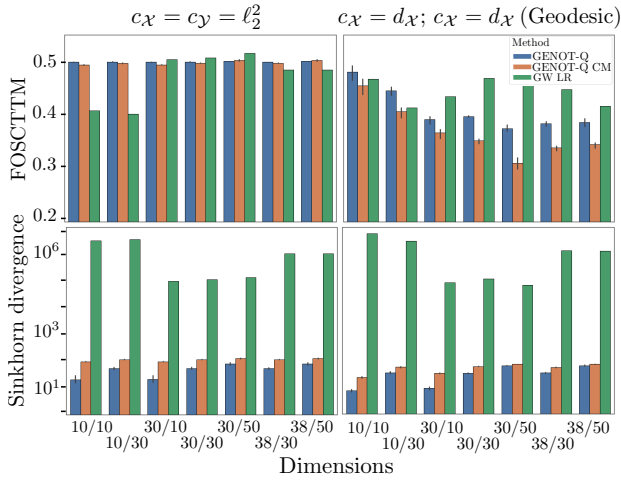


Figure 8. Benchmark of GENOT-Q models against discrete GW (GW-LR, App. E) on translating cells between ATAC space of dimension d_1 and RNA space of dimension d_2 . Performance is measured with the FOSCTTM score (App. B.2) and the Sinkhorn divergence between target and predicted target distribution. (left) intra-domain costs $c_X = c_Y = \ell_2^2$, (right) geodesic distances $c_X = d_X$ and $c_Y = d_Y$. Mean and 95% CI shown across 3 runs.

5.2. GENOT for Quadratic EOT Problems

GENOT-Q on simulated data. We transport a Swiss role in \mathbb{R}^3 to a spiral in \mathbb{R}^2 . Fig. 6 shows that GENOT-Q successfully mimics an isometric alignment. Here, we set $\varepsilon = 0.01$ and investigate its influence in more detail in Fig. 18.

GENOT-Q translates modalities of single cells. The number of modalities of a cell that can be simultaneously measured is limited due to technical limitations. Yet, it is important to match measurements of different modalities to obtain a more holistic view of the profile of a cell. Demetci et al. (2022) address this task using discrete quadratic OT. However, due to the lack of neural quadratic EOT solvers,

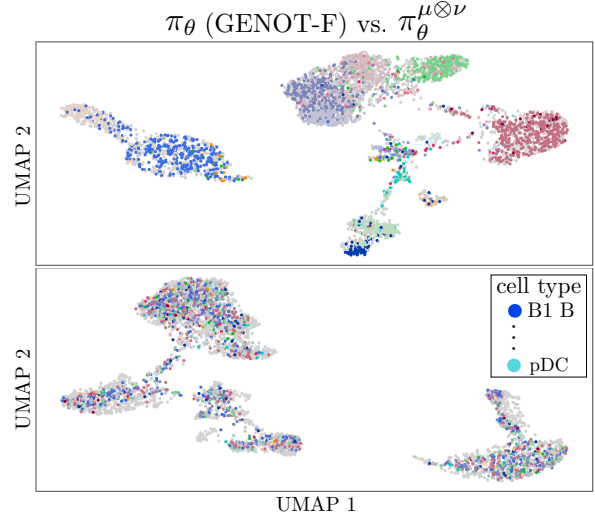


Figure 7. **Top:** UMAP of transported cells with GENOT-F (colored by cell type) and cells in the target distribution (gray). GENOT-F clusters similar cells together, i.e., according to their cell type. **Bottom:** UMAP of transported cells with a GENOT model trained on batch-wise independent couplings, thus not using OT. This remains to replace π_ε^* by $\mu \otimes \nu$ in Eq. (5). While the learned coupling then randomly mixes the cell types, it also degrades the global fitting of the target distribution of cells.

no OT-inspired method naturally allows for out-of-sample prediction. In the following, we use GENOT-Q to translate ATAC measurements (source) to gene expression space (target) on a bone marrow dataset (Luecken et al., 2021). As both modalities were measured in the same cell, the true match of each cell is known for this specific dataset. We compare GENOT-Q with discrete OT extended out-of-sample with linear regression (GW-LR, see E.2). We assess the performance using (i) the FOSCTTM (“Fractions of Samples Closer to the True Match”, see B.2) that measures the optimality of the learned coupling, and (ii) the Sinkhorn divergence (Feydy et al., 2019) between the predicted target and the target to assess distributional fitting. As in § 5.1, we leverage GENOT’s flexibility and use as intra-domain costs the geodesic distances on the source and target domain, namely $c_X = d_X$, $c_Y = d_Y$. We also estimate the EOT coupling for the ℓ_2^2 cost for comparison. Results are shown in Fig. 8. Regarding the FOSCTTM score, we can see that (i) using geodesic costs is crucial in high dimensions and (ii) GW-LR is competitive in low dimensions but not for higher ones. Regarding distributional fitting, GENOT models outperform by orders of magnitude.

GENOT-F improves modality translation. To enhance the performances attained by purely quadratic OT-based models, we introduce a novel method for translating between ATAC and RNA. We extend the idea proposed by Demetci et al. (2022) to the fused setting: We approximate RNA data from ATAC measurements using gene activity (Stuart et al., 2021), and we further process the data using a conditional

VAE (Lopez et al., 2018a) to reduce batch effects. This way, we construct a joint space Ω . Following the notations in § 3.3, RNA (source $\mathbf{x} \in \tilde{\mathcal{X}}$) and ATAC (target $\mathbf{y} \in \tilde{\mathcal{Y}}$) carry the structural information, while features $\mathbf{u} \in \Omega$ and $\mathbf{v} \in \Omega$ are obtained from the VAE embedding. Fig. 19 shows that the additional linear penalty on the feature term helps to obtain a better alignment compared to GENOT-Q. Fig. 7 visualizes the learned fused coupling compared to GENOT trained with batch-wise independent couplings. When aligning multiple modalities of single cells, the proportions of cell types in the two modalities might differ. We simulate this setting by removing cells belonging to certain cell types Tab. 4 shows that U-GENOT-F preserves high accuracy while learning meaningful rescaling functions.

Conclusion. We introduce GENOT, a versatile neural OT framework to learn cost-efficient stochastic maps, within the same space, or across incomparable spaces. We can loosen the mass conservation constraint if desired, while transport plans can be learned using any cost. We demonstrate that GENOT’s flexibility meets numerous requirements necessary for various prominent tasks in single-cell biology. GENOT models are implemented in `ott-jax` (Cuturi et al., 2022).

Impact Statement. This work introduces novel approaches in neural optimal transport and presents applications in single-cell biology. Leveraging single-cell genomics data holds promise for advancing personalized medicine but requires cautious handling due to its potential inclusion of sensitive information. Moreover, as neural optimal transport techniques find applicability across diverse domains, the societal ramifications of this research extend beyond single-cell genomics. With our publicly available implementation of GENOT in `ott-jax` (Cuturi et al., 2022), we enable its utilization by general machine learning practitioners. In a planned future release in `moscot` (Klein et al., 2023), we ensure GENOT’s accessibility to advance and accelerate research specifically tailored for single-cell biologists.

Acknowledgement. Co-funded by the European Union (ERC, DeepCell - 101054957). Views and opinions expressed are, however, those of the author(s) only and do not necessarily reflect those of the European Union or the European Research Council. Neither the European Union nor the granting authority can be held responsible for them. F.J.T. consults for Immunai Inc., Singularity Bio B.V., CytoReason Ltd, Cellarity, and has ownership interest in Dermagnostix GmbH and Cellarity.

References

Alvarez-Melis, D. and Jaakkola, T. S. Gromov-wasserstein alignment of word embedding spaces. *arXiv preprint arXiv:1809.00013*, 2018.

Asadulaev, A., Korotin, A., Egiazarian, V., and Burnaev, E. Neural optimal transport with general cost functionals, 2022. URL <https://arxiv.org/abs/2205.15403>.

Balaji, Y., Chellappa, R., and Feizi, S. Robust optimal transport with applications in generative modeling and domain adaptation. *Advances in Neural Information Processing Systems*, 33:12934–12944, 2020.

Bastidas-Ponce, A., Tritschler, S., Dony, L., Scheibner, K., Tarquis-Medina, M., Salinno, C., Schirge, S., Burtscher, I., Böttcher, A., Theis, F. J., et al. Comprehensive single cell mrna profiling reveals a detailed roadmap for pancreatic endocrinogenesis. *Development*, 146(12):dev173849, 2019.

Benamou, J.-D. Numerical resolution of an “unbalanced” mass transport problem. *ESAIM: Mathematical Modelling and Numerical Analysis*, 37(05):851–868, 2003.

Benamou, J.-D., Carlier, G., and Nenna, L. A numerical method to solve optimal transport problems with coulomb cost, 2015.

Bortoli, V. D., Liu, G.-H., Chen, T., Theodorou, E. A., and Nie, W. Augmented bridge matching, 2023.

Bradbury, J., Frostig, R., Hawkins, P., Johnson, M. J., Leary, C., Maclaurin, D., Necula, G., Paszke, A., VanderPlas, J., Wanderman-Milne, S., and Zhang, Q. JAX: composable transformations of Python+NumPy programs, 2018. URL <http://github.com/google/jax>.

Bunne, C., Stark, S. G., Gut, G., del Castillo, J. S., Lehmann, K.-V., Pelkmans, L., Krause, A., and Ratsch, G. Learning Single-Cell Perturbation Responses using Neural Optimal Transport. *bioRxiv*, 2021.

Bunne, C., Krause, A., and Cuturi, M. Supervised training of conditional monge maps. In *Advances in Neural Information Processing Systems (NeurIPS)*, 2022.

Chen, R. T., Rubanova, Y., Bettencourt, J., and Duvenaud, D. K. Neural ordinary differential equations. *Advances in neural information processing systems*, 31, 2018.

Chen, T., Liu, G.-H., and Theodorou, E. A. Likelihood training of schrödinger bridge using forward-backward sdes theory. *arXiv preprint arXiv:2110.11291*, 2021.

Chizat, L., Peyré, G., Schmitzer, B., and Vialard, F.-X. Unbalanced optimal transport: geometry and Kantorovich formulation. *Journal of Functional Analysis*, 274(11): 3090–3123, 2018.

Crane, K., Weischedel, C., and Wardetzky, M. Geodesics in heat: A new approach to computing distance based on

- heat flow. *ACM Transactions on Graphics (TOG)*, 32(5): 1–11, 2013.
- Cuturi, M. Sinkhorn Distances: Lightspeed Computation of Optimal Transport. In *Advances in Neural Information Processing Systems (NeurIPS)*, volume 26, 2013.
- Cuturi, M., Meng-Papaxanthos, L., Tian, Y., Bunne, C., Davis, G., and Teboul, O. Optimal Transport Tools (OTT): A JAX Toolbox for all things Wasserstein. *arXiv Preprint arXiv:2201.12324*, 2022.
- Daniels, M., Maunu, T., and Hand, P. Score-based generative neural networks for large-scale optimal transport. *Advances in neural information processing systems*, 34: 12955–12965, 2021.
- De Bortoli, V., Thornton, J., Heng, J., and Doucet, A. Diffusion schrödinger bridge with applications to score-based generative modeling. *Advances in Neural Information Processing Systems*, 34:17695–17709, 2021.
- Demetci, P., Santorella, R., Sandstede, B., Noble, W. S., and Singh, R. Scot: single-cell multi-omics alignment with optimal transport. *Journal of Computational Biology*, 29(1):3–18, 2022.
- Elowitz, M. B., Levine, A. J., Siggia, E. D., and Swain, P. S. Stochastic gene expression in a single cell. *Science*, 297(5584):1183–1186, 2002.
- Eyring, L., Klein, D., Uscidda, T., Palla, G., Kilbertus, N., Akata, Z., and Theis, F. Unbalancedness in neural monge maps improves unpaired domain translation. *arXiv preprint arXiv:2311.15100*, 2023.
- Eyring, L. V., Klein, D., Palla, G., Becker, S., Weiler, P., Kilbertus, N., and Theis, F. J. Modeling single-cell dynamics using unbalanced parameterized monge maps. *bioRxiv*, 2022. doi: 10.1101/2022.10.04.510766. URL <https://www.biorxiv.org/content/early/2022/10/05/2022.10.04.510766>.
- Fan, J., Taghvaei, A., and Chen, Y. Scalable computations of wasserstein barycenter via input convex neural networks. *arXiv preprint arXiv:2007.04462*, 2020.
- Fatras, K., Zine, Y., Majewski, S., Flamary, R., Gribonval, R., and Courty, N. Minibatch optimal transport distances; analysis and applications. *arXiv preprint arXiv:2101.01792*, 2021.
- Feydy, J., Séjourné, T., Vialard, F.-X., Amari, S.-I., Trounev, A., and Peyré, G. Interpolating between Optimal Transport and MMD using Sinkhorn Divergences. In *International Conference on Artificial Intelligence and Statistics (AISTATS)*, volume 22, 2019.
- Frogner, C., Zhang, C., Mobahi, H., Araya, M., and Poggio, T. A. Learning with a wasserstein loss. *Advances in neural information processing systems*, 28, 2015.
- Gayoso, A., Weiler, P., Lotfollahi, M., Klein, D., Hong, J., Streets, A. M., Theis, F. J., and Yosef, N. Deep generative modeling of transcriptional dynamics for rna velocity analysis in single cells. *bioRxiv*, pp. 2022–08, 2022.
- Genevay, A., Chizat, L., Bach, F., Cuturi, M., and Peyré, G. Sample Complexity of Sinkhorn Divergences. In *International Conference on Artificial Intelligence and Statistics (AISTATS)*, volume 22, 2019a.
- Genevay, A., Chizat, L., Bach, F., Cuturi, M., and Peyré, G. Sample complexity of sinkhorn divergences. In *The 22nd international conference on artificial intelligence and statistics*, pp. 1574–1583. PMLR, 2019b.
- Gushchin, N., Kolesov, A., Korotin, A., Vetrov, D., and Burnaev, E. Entropic neural optimal transport via diffusion processes. *arXiv preprint arXiv:2211.01156*, 2022.
- Gushchin, N., Kolesov, A., Mokrov, P., Karpikova, P., Spiridonov, A., Burnaev, E., and Korotin, A. Building the bridge of schrödinger: A continuous entropic optimal transport benchmark. *arXiv preprint arXiv:2306.10161*, 2023.
- Haniffa, M., Taylor, D., Linnarsson, S., Aronow, B. J., Bader, G. D., Barker, R. A., Camara, P. G., Camp, J. G., Chédotal, A., Copp, A., et al. A roadmap for the human developmental cell atlas. *Nature*, 597(7875):196–205, 2021.
- He, Z., Dony, L., Fleck, J. S., Szalata, A., Li, K. X., Sliskovic, I., Lin, H.-C., Santel, M., Atamian, A., Quadrato, G., et al. An integrated transcriptomic cell atlas of human neural organoids. *bioRxiv*, pp. 2023–10, 2023.
- Hetzl, L., Boehm, S., Kilbertus, N., Günnemann, S., Theis, F., et al. Predicting cellular responses to novel drug perturbations at a single-cell resolution. *Advances in Neural Information Processing Systems*, 35:26711–26722, 2022.
- Heumos, L., Schaar, A. C., Lance, C., Litinetskaya, A., Drost, F., Zappia, L., Lücken, M. D., Strobl, D. C., Henao, J., Curion, F., et al. Best practices for single-cell analysis across modalities. *Nature Reviews Genetics*, pp. 1–23, 2023.
- Huguet, G., Tong, A., Zapatero, M. R., Wolf, G., and Krishnaswamy, S. Geodesic sinkhorn: optimal transport for high-dimensional datasets. *arXiv preprint arXiv:2211.00805*, 2022.

- Kallenberg, O. *Foundations of Modern Probability*. Springer, 2002. URL <https://link.springer.com/book/10.1007/978-3-030-61871-1>.
- Kantorovich, L. On the transfer of masses (in russian). In *Doklady Akademii Nauk*, volume 37, pp. 227, 1942.
- Klein, D., Palla, G., Lange, M., Klein, M., Piran, Z., Gander, M., Meng-Papaxanthos, L., Sterr, M., Bastidas-Ponce, A., Tarquis-Medina, M., et al. Mapping cells through time and space with moscot. *bioRxiv*, pp. 2023–05, 2023.
- Korotin, A., Egiazarian, V., Asadulaev, A., Safin, A., and Burnaev, E. Wasserstein-2 generative networks. In *International Conference on Learning Representations*, 2020.
- Korotin, A., Selikhanovych, D., and Burnaev, E. Neural optimal transport. 2022. doi: 10.48550/ARXIV.2201.12220. URL <https://arxiv.org/abs/2201.12220>.
- Korotin, A., Gushchin, N., and Burnaev, E. Light schrödinger bridge, 2023a.
- Korotin, A., Selikhanovych, D., and Burnaev, E. Kernel neural optimal transport, 2023b.
- Lange, M., Piran, Z., Klein, M., Spanjaard, B., Klein, D., Junker, J. P., Theis, F. J., and Nitzan, M. Mapping lineage-traced cells across time points with moslin. *bioRxiv*, pp. 2023–04, 2023.
- Liero, M., Mielke, A., and Savaré, G. Optimal entropy-transport problems and a new hellinger–kantorovich distance between positive measures. *Inventiones Mathematicae*, 211(3):969–1117, 2018.
- Lipman, Y., Chen, R. T. Q., Ben-Hamu, H., Nickel, M., and Le, M. Flow matching for generative modeling, 2023.
- Liu, G.-H., Vahdat, A., Huang, D.-A., Theodorou, E. A., Nie, W., and Anandkumar, A. I²sb: Image-to-image schrödinger bridge, 2023.
- Liu, X., Gong, C., and Liu, Q. Flow straight and fast: Learning to generate and transfer data with rectified flow, 2022.
- Lopez, R., Regier, J., Cole, M. B., Jordan, M. I., and Yosef, N. Deep generative modeling for single-cell transcriptomics. *Nature methods*, 15(12):1053–1058, 2018a.
- Lopez, R., Regier, J., Cole, M. B., Jordan, M. I., and Yosef, N. Deep generative modeling for single-cell transcriptomics. *Nature methods*, 15(12), 2018b.
- Lübeck, F., Bunne, C., Gut, G., del Castillo, J. S., Pelkmans, L., and Alvarez-Melis, D. Neural unbalanced optimal transport via cycle-consistent semi-couplings. *arXiv preprint arXiv:2209.15621*, 2022.
- Luecken, M. D., Burkhardt, D. B., Cannoodt, R., Lance, C., Agrawal, A., Aliee, H., Chen, A. T., Deconinck, L., Detweiler, A. M., Granados, A. A., et al. A sandbox for prediction and integration of dna, rna, and proteins in single cells. In *Thirty-fifth conference on neural information processing systems datasets and benchmarks track (Round 2)*, 2021.
- Léonard, C. A survey of the schrödinger problem and some of its connections with optimal transport, 2013.
- Makkuva, A., Taghvaei, A., Oh, S., and Lee, J. Optimal transport mapping via input convex neural networks. In *International Conference on Machine Learning (ICML)*, volume 37, 2020.
- McInnes, L., Healy, J., and Melville, J. Umap: Uniform manifold approximation and projection for dimension reduction. *arXiv preprint arXiv:1802.03426*, 2018.
- Mémoli, F. Gromov–wasserstein distances and the metric approach to object matching. *Foundations of computational mathematics*, 11:417–487, 2011.
- Mokrov, P., Korotin, A., and Burnaev, E. Energy-guided entropic neural optimal transport. *arXiv preprint arXiv:2304.06094*, 2023.
- Monge, G. Mémoire sur la théorie des déblais et des remblais. *Histoire de l’Académie Royale des Sciences*, pp. 666–704, 1781.
- Moon, K. R., Stanley III, J. S., Burkhardt, D., van Dijk, D., Wolf, G., and Krishnaswamy, S. Manifold learning-based methods for analyzing single-cell rna-sequencing data. *Current Opinion in Systems Biology*, 7:36–46, 2018.
- Nekrashevich, M., Korotin, A., and Burnaev, E. Neural gromov-wasserstein optimal transport. *arXiv preprint arXiv:2303.05978*, 2023.
- Nitzan, M., Karaiskos, N., Friedman, N., and Rajewsky, N. Gene expression cartography. *Nature*, 576(7785): 132–137, 2019.
- Nutz, M. Introduction to entropic optimal transport.
- Peluchetti, S. Diffusion bridge mixture transports, schrödinger bridge problems and generative modeling, 2023.
- Peyré, G., Cuturi, M., and Solomon, J. Gromov-wasserstein averaging of kernel and distance matrices. In *International Conference on Machine Learning*, pp. 2664–2672, 2016.
- Pooladian, A.-A. and Niles-Weed, J. Entropic estimation of optimal transport maps. *arXiv preprint arXiv:2109.12004*, 2021.

- Pooladian, A.-A., Ben-Hamu, H., Domingo-Enrich, C., Amos, B., Lipman, Y., and Chen, R. Multisample flow matching: Straightening flows with minibatch couplings. *arXiv preprint arXiv:2304.14772*, 2023.
- Rigollet, P. and Stromme, A. J. On the sample complexity of entropic optimal transport, 2022.
- Rioux, G., Goldfeld, Z., and Kato, K. Entropic gromov-wasserstein distances: Stability, algorithms, and distributional limits. *arXiv preprint arXiv:2306.00182*, 2023.
- Santambrogio, F. Optimal Transport for Applied Mathematicians. *Birkhäuser, NY*, 55(58-63):94, 2015.
- Scetbon, M., Cuturi, M., and Peyré, G. Low-rank sinkhorn factorization. In *International Conference on Machine Learning*, pp. 9344–9354. PMLR, 2021.
- Scetbon, M., Peyré, G., and Cuturi, M. Linear-time gromov wasserstein distances using low rank couplings and costs. In *International Conference on Machine Learning*, pp. 19347–19365. PMLR, 2022.
- Schiebinger, G., Shu, J., Tabaka, M., Cleary, B., Subramanian, V., Solomon, A., Gould, J., Liu, S., Lin, S., Berube, P., et al. Optimal-Transport Analysis of Single-Cell Gene Expression Identifies Developmental Trajectories in Reprogramming. *Cell*, 176(4), 2019.
- Seguy, V., Damodaran, B. B., Flamary, R., Courty, N., Rolet, A., and Blondel, M. Large-scale optimal transport and mapping estimation. *arXiv preprint arXiv:1711.02283*, 2017.
- Séjourné, T., Vialard, F.-X., and Peyré, G. The unbalanced gromov wasserstein distance: Conic formulation and relaxation. *Advances in Neural Information Processing Systems*, 34:8766–8779, 2021.
- Shi, Y., De Bortoli, V., Campbell, A., and Doucet, A. Diffusion schrödinger bridge matching. *arXiv preprint arXiv:2303.16852*, 2023.
- Solomon, J., De Goes, F., Peyré, G., Cuturi, M., Butscher, A., Nguyen, A., Du, T., and Guibas, L. Convolutional wasserstein distances: Efficient optimal transportation on geometric domains. *ACM Transactions on Graphics (ToG)*, 34(4):1–11, 2015.
- Srivatsan, S. R., McFaline-Figueroa, J. L., Ramani, V., Saunders, L., Cao, J., Packer, J., Pliner, H. A., Jackson, D. L., Daza, R. M., Christiansen, L., et al. Massively multiplex chemical transcriptomics at single-cell resolution. *Science*, 367(6473), 2020.
- Stuart, T., Srivastava, A., Madad, S., Lareau, C. A., and Satija, R. Single-cell chromatin state analysis with signac. *Nature methods*, 18(11):1333–1341, 2021.
- Sturm, K.-T. The space of spaces: curvature bounds and gradient flows on the space of metric measure spaces, 2020.
- Séjourné, T., Peyré, G., and Vialard, F.-X. Unbalanced optimal transport, from theory to numerics, 2023a.
- Séjourné, T., Vialard, F.-X., and Peyré, G. The unbalanced gromov wasserstein distance: Conic formulation and relaxation, 2023b.
- Thual, A., Tran, H., Zemsanova, T., Courty, N., Flamary, R., Dehaene, S., and Thirion, B. Aligning individual brains with fused unbalanced gromov-wasserstein, 2023.
- Tong, A., Huang, J., Wolf, G., Van Dijk, D., and Krishnaswamy, S. TrajectoryNet: A Dynamic Optimal Transport Network for Modeling Cellular Dynamics. In *International Conference on Machine Learning (ICML)*, 2020.
- Tong, A., Malkin, N., Fatras, K., Atanackovic, L., Zhang, Y., Hugué, G., Wolf, G., and Bengio, Y. Simulation-free schrödinger bridges via score and flow matching. *arXiv preprint arXiv:2307.03672*, 2023a.
- Tong, A., Malkin, N., Hugué, G., Zhang, Y., Rector-Brooks, J., Fatras, K., Wolf, G., and Bengio, Y. Conditional flow matching: Simulation-free dynamic optimal transport. *arXiv preprint arXiv:2302.00482*, 2023b.
- Uscidda, T. and Cuturi, M. The monge gap: A regularizer to learn all transport maps, 2023.
- Vargas, F., Thodoroff, P., Lamacraft, A., and Lawrence, N. Solving schrödinger bridges via maximum likelihood. *Entropy*, 23(9):1134, 2021.
- Vayer, T., Chapel, L., Flamary, R., Tavenard, R., and Courty, N. Optimal transport for structured data with application on graphs. *arXiv preprint arXiv:1805.09114*, 2018.
- Weed, J. and Bach, F. Sharp asymptotic and finite-sample rates of convergence of empirical measures in wasserstein distance, 2017. URL <https://arxiv.org/abs/1707.00087>.
- Yang, K. D. and Uhler, C. Scalable Unbalanced Optimal Transport using Generative Adversarial Networks. *International Conference on Learning Representations (ICLR)*, 2019.
- Zeira, R., Land, M., Strzalkowski, A., and Raphael, B. J. Alignment and integration of spatial transcriptomics data. *Nature Methods*, 19(5):567–575, 2022.
- Zhang, Z., Goldfeld, Z., Mroueh, Y., and Sriperumbudur, B. K. Gromov-wasserstein distances: Entropic regularization, duality, and sample complexity, 2023.

Zhou, L., Lou, A., Khanna, S., and Ermon, S. Denoising diffusion bridge models, 2023.

Appendix

A. Proofs

A.1. Proofs of § 3.1

Proposition 3.1 (Well-posedness of GENOT.). *Suppose that $\mathcal{L}_{\text{GENOT}}(\theta) = 0$. Then, for $X \sim \mu$, $Z \sim \rho$ and $Y = \phi_1(Z|X)$ denoting the solution of ODE (3), one has $Y \sim \pi_\varepsilon^*(\cdot|X)$, and hence $(X, Y) \sim \pi_\varepsilon^*$.*

Proof. This result follows directly from the construction of the loss. Suppose that $\mathcal{L}_{\text{GENOT}}(\theta) = 0$. By Fubini's Theorem, this implies that:

$$\begin{aligned} & \mathbb{E}_{X \sim \mu} \mathbb{E}_{t \sim \mathcal{U}([0,1]), Z \sim \rho, Y \sim \pi_\varepsilon^*(\cdot|X)} [\|v_{t,\theta}([Z, Y]_t|X) - (Y - Z)\|_2^2] = 0. \\ \text{i.e. } & \mathbb{E}_{X \sim \mu} \mathbb{E}_{t \sim \mathcal{U}([0,1]), Z \sim \rho, Y \sim \pi_\varepsilon^*(\cdot|X)} [\|v_{t,\theta}(tZ + (1-t)Y|X) - (Y - Z)\|_2^2] = 0. \end{aligned} \quad (6)$$

Since it is positive, the function

$$\ell : \mathbf{x} \mapsto \mathbb{E}_{t \sim \mathcal{U}([0,1]), Z \sim \rho, Y \sim \pi_\varepsilon^*(\cdot|\mathbf{x})} [\|v_{t,\theta}(tZ + (1-t)Y|\mathbf{x}) - (Y - Z)\|_2^2]$$

is therefore zero μ -a.e., which means that for any \mathbf{x} in the support of μ , one has $\ell(\mathbf{x}) = 0$. Moreover, $\ell(\mathbf{x})$ is the CFM loss with source ρ and target $\pi_\varepsilon^*(\cdot|\mathbf{x})$, applied to the vector field $v_{t,\theta}(\cdot|\mathbf{x})$. Therefore, $\ell(\mathbf{x}) = 0$ implies that $v_{t,\theta}(\cdot|\mathbf{x})$ generates a probability path between ρ and $\pi_\varepsilon^*(\cdot|\mathbf{x})$ thanks to (Lipman et al., 2023, Theorem 1). This means that if $\phi_t(\cdot|\mathbf{x})$ is the flow induced by $v_{t,\theta}(\cdot|\mathbf{x})$, one has $\phi_1(\cdot|\mathbf{x})\#\rho = \pi_\varepsilon^*(\cdot|\mathbf{x})$. Afterwards, if $X \sim \mu$, $Z \sim \rho$ and $Y = \phi_1(Z|X)$ denotes the solution of ODE (3), one has $Y \sim \pi_\varepsilon^*(\cdot|X)$, so $(X, Y) \sim \pi_\varepsilon^*$ by definition. \square

Proposition 3.2 (Re-Balancing the unbalanced problems.). *Let $\pi_{\varepsilon,\tau}^*$ be an unbalanced EOT coupling, solution of (ULEOT) or (UQEOT) between $\mu \in \mathcal{M}^+(\mathcal{X})$ and $\nu \in \mathcal{M}^+(\mathcal{Y})$. We note $\tilde{\mu} = p_1\#\pi_{\varepsilon,\tau}^*$ and $\tilde{\nu} = p_2\#\pi_{\varepsilon,\tau}^*$ its marginals. Then, in both cases, $\tilde{\mu}$ (resp. $\tilde{\nu}$) has a density w.r.t μ (resp. ν) i.e. it exists $\eta, \xi : \mathbb{R}^d \rightarrow \mathbb{R}^+$ s.t. $\tilde{\mu} = \eta \cdot \mu$ and $\tilde{\nu} = \xi \cdot \nu$. Moreover, $\tilde{\mu}$ and $\tilde{\nu}$ have the same mass and*

1. (Linear) $\pi_{\varepsilon,\tau}^*$ solves the balanced problem (LEOT) between $\tilde{\mu}$ and $\tilde{\nu}$ with the same ε .
2. (Quadratic) Provided that $c_{\mathcal{X}}$ and $c_{\mathcal{Y}}$ (or $-c_{\mathcal{X}}$ and $-c_{\mathcal{Y}}$) are conditionally positive kernels (see Def. A.1), $\pi_{\varepsilon,\tau}^*$ solves the balanced problem (QEOT) between $\tilde{\mu}$ and $\tilde{\nu}$ with $\varepsilon' = m(\pi_{\varepsilon,\tau}^*) \varepsilon$, where $m(\pi_{\varepsilon,\tau}^*) = \pi_{\varepsilon,\tau}^*(\mathcal{X} \times \mathcal{Y})$.

We first remind the definition of a conditionally positive kernel, which is involved in point 2. of Prop. 3.2.

Definition A.1. A kernel $k : \mathbb{R}^d \times \mathbb{R}^d \rightarrow \mathbb{R}$ is conditionally positive if it is symmetric and for any $\mathbf{x}_1, \dots, \mathbf{x}_n \in \mathbb{R}^d$ and $\mathbf{a} \in \mathbb{R}^n$ s.t. $\mathbf{a}^\top \mathbf{1}_n = 0$, one has

$$\sum_{i,j=1}^n a_i a_j k(\mathbf{x}_i, \mathbf{x}_j) \geq 0$$

Conditionally positive kernels include all positive kernels, such $k(\mathbf{x}, \mathbf{y}) = \langle \mathbf{x}, \mathbf{y} \rangle$ or $k_\gamma(\mathbf{x}, \mathbf{y}) = \exp(-\frac{1}{\gamma} \|\mathbf{x} - \mathbf{y}\|_2^2)$, but also the negative squared Euclidean distance $k(\mathbf{x}, \mathbf{y}) = -\|\mathbf{x} - \mathbf{y}\|_2^2$.

Proof of 3.2. Step 1: Re-weightings. We first show that for $\pi_{\varepsilon,\tau}^*$ solution of (LEOT) or (QEOT), it exists $\eta, \xi : \mathbb{R}^d \rightarrow \mathbb{R}^+$ s.t. $\tilde{\mu} = p_1\#\pi_{\varepsilon,\tau}^* = \eta \cdot \mu$ and $\tilde{\nu} = p_2\#\pi_{\varepsilon,\tau}^* = \xi \cdot \nu$.

We start with the linear case and consider $\pi_{\varepsilon,\tau}^*$ solution of (LEOT). The result follows from duality. Indeed, from (Séjourné et al., 2023a, Prop. 2), one has the existence of the so-called entropic potentials $f^* \in \mathcal{C}(\mathcal{X})$ and $g^* \in \mathcal{C}(\mathcal{Y})$ s.t.

$$\frac{d\pi_{\varepsilon,\tau}^*}{d(\mu \otimes \nu)}(\mathbf{x}, \mathbf{y}) = \exp\left(\frac{f^*(\mathbf{x}) + g^*(\mathbf{y}) - c(\mathbf{x}, \mathbf{y})}{\varepsilon}\right) \quad (7)$$

Therefore, $\tilde{\mu} = \eta \cdot \mu$ and $\tilde{\nu} = \xi \cdot \nu$ where $\eta : \mathcal{X} \rightarrow \mathbb{R}^+$ and $\xi : \mathcal{Y} \rightarrow \mathbb{R}^+$ are defined by:

$$\eta(\mathbf{x}) = \int_{\mathcal{Y}} \exp\left(\frac{f^*(\mathbf{x}) + g^*(\mathbf{y}) - c(\mathbf{x}, \mathbf{y})}{\varepsilon}\right) d\nu(\mathbf{y}) \quad \text{and} \quad \xi(\mathbf{y}) = \int_{\mathcal{X}} \exp\left(\frac{f^*(\mathbf{x}) + g^*(\mathbf{y}) - c(\mathbf{x}, \mathbf{y})}{\varepsilon}\right) d\mu(\mathbf{x}). \quad (8)$$

We now handle the quadratic case and consider $\pi_{\varepsilon, \tau}^*$ solution of (UQEOT). We remind that the (UQEOT) problem between μ and ν reads:

$$\min_{\pi \in \mathcal{M}^+(\mathcal{X} \times \mathcal{Y})} \int_{(\mathcal{X} \times \mathcal{Y})^2} |c_{\mathcal{X}}(\mathbf{x}, \mathbf{x}') - c_{\mathcal{Y}}(\mathbf{y}, \mathbf{y}')|^2 d\pi(\mathbf{x}, \mathbf{y}) d\pi(\mathbf{x}', \mathbf{y}') + \varepsilon \text{KL}^{\otimes}(\pi | \mu \otimes \nu) + \lambda_1 \text{KL}^{\otimes}(\pi_1 | \mu) + \lambda_2 \text{KL}^{\otimes}(\pi_2 | \nu),$$

For $\pi \in \mathcal{M}^+(\mathcal{X} \times \mathcal{Y})$, the quadratic relative entropy $\text{KL}^{\otimes}(\pi | \mu \otimes \nu) = \text{KL}(\pi \otimes \pi | (\mu \otimes \nu) \otimes (\mu \otimes \nu))$ is finite i.f.f. $\pi \otimes \pi$ has a density w.r.t. $(\mu \otimes \nu) \otimes (\mu \otimes \nu)$, which implies that π has a density w.r.t. $\mu \otimes \nu$. Therefore, one can reformulate (UQEOT) as:

$$\begin{aligned} \min_{h \in L_1^+(\mathcal{X} \times \mathcal{Y})} \int_{(\mathcal{X} \times \mathcal{Y})^2} (c_{\mathcal{X}}(\mathbf{x}, \mathbf{x}') - c_{\mathcal{Y}}(\mathbf{y}, \mathbf{y}'))^2 h(\mathbf{x}, \mathbf{y}) h(\mathbf{x}', \mathbf{y}') d\mu(\mathbf{x}) d\mu(\mathbf{x}') d\nu(\mathbf{y}) d\nu(\mathbf{y}') \\ + \varepsilon \text{KL}(h | \mu \otimes \nu) + \tau_1 \text{KL}(h_1 | \mu) + \tau_2 \text{KL}(h_2 | \nu) \end{aligned} \quad (9)$$

where we extend the KL divergence for densities: $\text{KL}(r | \gamma) = \int (r \log(r) + r - 1) d\gamma$, and define the marginal densities $h_1 : \mathbf{x} \in \mathcal{X} \mapsto \int_{\mathcal{Y}} h(\mathbf{x}, \mathbf{y}) d\nu(\mathbf{y})$ and $h_2 : \mathbf{y} \in \mathcal{Y} \mapsto \int_{\mathcal{X}} h(\mathbf{x}, \mathbf{y}) d\mu(\mathbf{x})$. As a result, it exists $h^* \in L_1^+(\mathcal{X} \times \mathcal{Y})$ s.t. $\pi_{\varepsilon, \tau}^* = h^* \cdot \mu \otimes \nu$. It follows that $\tilde{\mu} = \eta \cdot \mu$ and $\tilde{\nu} = \xi \cdot \nu$ with $\eta = h_1^*$ and $\xi = h_2^*$.

Remark A.2. Note that in both cases, since $d\tilde{\mu}(\mathbf{x}) = \eta(\mathbf{x}) d\mu(\mathbf{x})$ and $d\tilde{\nu}(\mathbf{y}) = \xi(\mathbf{y}) d\nu(\mathbf{y})$, the equality of mass of $\tilde{\mu}$ and $\tilde{\nu}$ yields $\mathbb{E}_{X \sim \mu}[\eta(X)] = \mathbb{E}_{Y \sim \nu}[\xi(Y)]$.

Step 2: Optimality in the balanced problem for the linear case. We now prove **point 1**, stating that if $\pi_{\varepsilon, \tau}^*$ solves problem ULEOT between μ and ν , then it solves problem (LEOT) between $\tilde{\mu}$ and $\tilde{\nu}$ for the same entropic regularization strength ε . It also follows from duality. We remind that that thanks to (Séjourné et al., 2023a, Prop. 2)

$$\frac{d\pi_{\varepsilon, \tau}^*}{d(\mu \otimes \nu)}(\mathbf{x}, \mathbf{y}) = \exp\left(\frac{f^*(\mathbf{x}) + g^*(\mathbf{y}) - c(\mathbf{x}, \mathbf{y})}{\varepsilon}\right) \quad (10)$$

with $f^* \in \mathcal{C}(\mathcal{X})$ and $g^* \in \mathcal{C}(\mathcal{Y})$. Moreover, by (Nutz, Theorem 4.2), such a decomposition is equivalent to the optimality in problem (LEOT). Therefore, $\pi_{\varepsilon, \tau}^*$ solves problem LEOT between its marginals $\tilde{\mu}$ and $\tilde{\nu}$, i.e.

$$\pi_{\varepsilon, \tau}^* = \arg \min_{\pi \in \Pi(\tilde{\mu}, \tilde{\nu})} \int_{\mathcal{X} \times \mathcal{Y}} c(\mathbf{x}, \mathbf{y}) d\pi(\mathbf{x}, \mathbf{y}) + \varepsilon \text{KL}(\pi | \mu \otimes \nu). \quad (11)$$

Step 3: Optimality in the balanced problem for the quadratic case. We now prove **point 2**, stating that, provided that the costs $c_{\mathcal{X}}$ and $c_{\mathcal{Y}}$ are conditionally positive (or conditionally negative), if $\pi_{\varepsilon, \tau}^*$ solves problem (UQEOT) between μ and ν , then it actually solves problem (QEOT) between $\tilde{\mu}$ and $\tilde{\nu}$ for the entropic regularization strength $\varepsilon' = m(\pi_{\varepsilon, \tau}^*) \varepsilon$. We first define the functional:

$$\begin{aligned} F : (\gamma, \pi) \in \mathcal{M}^+(\mathcal{X} \times \mathcal{Y})^2 \mapsto \int_{(\mathcal{X} \times \mathcal{Y})^2} |c_{\mathcal{X}}(\mathbf{x}, \mathbf{x}') - c_{\mathcal{Y}}(\mathbf{y}, \mathbf{y}')|^2 d\pi(\mathbf{x}, \mathbf{y}) d\gamma(\mathbf{x}', \mathbf{y}') \\ + \varepsilon \text{KL}(\pi \otimes \gamma | (\mu \otimes \nu)^2) + \lambda_1 \text{KL}(\pi_1 \otimes \gamma_1 | \mu \times \mu) + \lambda_2 \text{KL}^{\otimes}(\pi_2 \otimes \gamma_2 | \nu \times \nu), \end{aligned} \quad (12)$$

s.t. $\pi_{\varepsilon, \tau}^* \in \arg \min_{\pi \in \mathcal{M}(\mathcal{X} \times \mathcal{Y})} F(\pi, \pi)$. Then, if we define the linearized cost

$$c_{\varepsilon, \tau}^* : (\mathbf{x}, \mathbf{y}) \in \mathcal{X} \times \mathcal{Y} \mapsto \int_{\mathcal{X} \times \mathcal{Y}} |c_{\mathcal{X}}(\mathbf{x}, \mathbf{x}') - c_{\mathcal{Y}}(\mathbf{y}, \mathbf{y}')|^2 d\pi_{\varepsilon, \tau}^*(\mathbf{x}', \mathbf{y}'), \quad (13)$$

we get from (Séjourné et al., 2023a, Proposition 9), that $\pi_{\varepsilon, \tau}^*$ solves:

$$\begin{aligned} \pi_{\varepsilon, \tau}^* \in \arg \min_{\pi \in \mathcal{M}(\mathcal{X} \times \mathcal{Y})} \int_{\mathcal{X} \times \mathcal{Y}} c_{\varepsilon, \tau}^*(\mathbf{x}, \mathbf{y}) d\pi(\mathbf{x}, \mathbf{y}) + \varepsilon m(\pi_{\varepsilon, \tau}^*) \text{KL}(\pi | \mu \otimes \nu) \\ + \lambda_1 m(\pi_{\varepsilon, \tau}^*) \text{KL}(\pi_1 | \mu) + \lambda_2 m(\pi_{\varepsilon, \tau}^*) \text{KL}(\pi_2 | \nu). \end{aligned} \quad (14)$$

Therefore, $\pi_{\varepsilon, \tau}^*$ solves problem ULEOT between μ and ν for a new cost $c_{\varepsilon, \tau}^*$, and the regularization strength $\varepsilon' = \varepsilon m(\pi_{\varepsilon, \tau}^*)$. We seek to apply point 1, to get that $\pi_{\varepsilon, \tau}^*$ solves problem LEOT between $\tilde{\mu} = p_1 \# \pi_{\varepsilon, \tau}^*$ and $\tilde{\nu} = p_2 \# \pi_{\varepsilon, \tau}^*$ for the same entropic

regularization strength ε' . To that end, we first verify that $c_{\varepsilon, \tau}^*$ is continuous. Since $c_{\mathcal{X}}$ and $c_{\mathcal{Y}}$ are continuous on $\mathcal{X} \times \mathcal{X}$ and $\mathcal{Y} \times \mathcal{Y}$, the function:

$$(\mathbf{x}, \mathbf{y}, \mathbf{x}', \mathbf{y}') \in (\mathcal{X} \times \mathcal{Y})^2 \mapsto |c_{\mathcal{X}}(\mathbf{x}, \mathbf{x}') - c_{\mathcal{Y}}(\mathbf{y}, \mathbf{y}')|^2$$

is continuous. Therefore, it is bounded since $(\mathcal{X} \times \mathcal{Y})^2$ is compact as a product of compact sets. Then, since $\pi_{\varepsilon, \tau}^*$ has finite mass, Lebesgue's dominated convergence yields the continuity of $c_{\varepsilon, \tau}^*$. We then to apply point 1 and get:

$$\pi_{\varepsilon, \tau}^* \in \arg \min_{\pi \in \Pi(\tilde{\mu}, \tilde{\nu})} \int_{\mathcal{X} \times \mathcal{Y}} c_{\varepsilon, \tau}^*(\mathbf{x}, \mathbf{y}) d\pi(\mathbf{x}, \mathbf{y}) + \varepsilon' \text{KL}(\pi | \mu \otimes \nu) \quad (15)$$

Since the costs are conditionally positive (or conditionally negative) kernels, (15) finally yields the desired result by applying (Séjourné et al., 2023b, Theorem 3):

$$\pi_{\varepsilon, \tau}^* \in \arg \min_{\pi \in \Pi(\tilde{\mu}, \tilde{\nu})} \int_{\mathcal{X} \times \mathcal{Y}} |c_{\mathcal{X}}(\mathbf{x}, \mathbf{x}') - c_{\mathcal{Y}}(\mathbf{y}, \mathbf{y}')| d\pi(\mathbf{x}', \mathbf{y}') d\pi(\mathbf{x}, \mathbf{y}) + \varepsilon' \text{KL}(\pi | \mu \otimes \nu) \quad (16)$$

Remark A.3. In various experimental settings, μ and ν have mass 1, and we impose one of the two hard marginal constraints, for instance, on μ , by setting $\tau_1 = 1$. Then $\tilde{\nu}$ has also mass 1 and $m(\pi_{\varepsilon, \tau}^*) = 1$, so $\varepsilon' = m(\pi_{\varepsilon, \tau}^*) = \varepsilon$ and we keep the same regularization strength ε by re-balancing (UQEOT). □

Proposition 3.3 (Pointwise estimation of re-weighting functions.). *Let $\pi_{\varepsilon, \tau}^n = \sum_{i,j} \mathbf{P}_{\varepsilon, \tau}^{i,j} \delta_{(X_i, Y_j)}$, solution to (ULEOT) between empirical counterparts of μ and ν . Let $\mathbf{a} = \mathbf{P}_{\varepsilon, \tau} \mathbf{1}_n$ and $\mathbf{b} = \mathbf{P}_{\varepsilon, \tau}^\top \mathbf{1}_n$ its marginals weights. Then, almost surely, $n a_i \rightarrow \eta(X_i)$ and $n b_i \rightarrow \xi(Y_i)$.*

Proof. As we saw in the proof of Prop.3.2, using Séjourné et al. (2023a, Prop. 2), one has the existence of $f^* \in C(\mathcal{X})$ and $g^* \in C(\mathcal{Y})$ s.t.

$$\frac{d\pi_{\varepsilon, \tau}^*}{d(\mu \otimes \nu)}(\mathbf{x}, \mathbf{y}) = \exp\left(\frac{f^*(\mathbf{x}) + g^*(\mathbf{y}) - c(\mathbf{x}, \mathbf{y})}{\varepsilon}\right) := h(\mathbf{x}, \mathbf{y})$$

and the relative densities η and ξ s.t. $\tilde{\mu} = p_1 \# \pi_{\varepsilon, \tau}^* = \eta \cdot \mu$ and $\tilde{\nu} = p_2 \# \pi_{\varepsilon, \tau}^* = \xi \cdot \nu$ are given by

$$\eta : \mathbf{x} \mapsto \int_{\mathcal{Y}} h(\mathbf{x}, \mathbf{y}) d\nu(\mathbf{y}) \quad \text{and} \quad \xi : \mathbf{y} \mapsto \int_{\mathcal{X}} h(\mathbf{x}, \mathbf{y}) d\mu(\mathbf{x}) \quad (17)$$

Now, let consider $\hat{\pi}_{\varepsilon, \tau} = \sum_{i,j} \mathbf{P}_{\varepsilon, \tau}^{i,j} \delta_{(X_i, Y_j)}$ the solution of problem LEOT between $\hat{\mu}_n = \frac{1}{n} \sum_{i=1}^n \delta_{X_i}$ and $\hat{\nu}_n = \frac{1}{n} \sum_{i=1}^n \delta_{Y_i}$. Similarly, using Séjourné et al. (2023a, Prop. 2), one has the existence of $f_n^* \in C(\mathcal{X})$ and $g_n^* \in C(\mathcal{Y})$ s.t.

$$\frac{d\hat{\pi}_{\varepsilon, \tau}}{d(\hat{\mu}_n \otimes \hat{\nu}_n)}(\mathbf{x}, \mathbf{y}) = \exp\left(\frac{f_n^*(\mathbf{x}) + g_n^*(\mathbf{y}) - c(\mathbf{x}, \mathbf{y})}{\varepsilon}\right) := h_n(\mathbf{x}, \mathbf{y}) \quad (18)$$

and the relative densities η_n and ξ_n s.t. $\tilde{\mu}_n = p_1 \# \hat{\pi}_{\varepsilon, \tau}^n = \eta_n \cdot \hat{\mu}_n$ and $\tilde{\nu}_n = p_2 \# \hat{\pi}_{\varepsilon, \tau}^n = \xi_n \cdot \hat{\nu}_n$ are given by

$$\eta_n : \mathbf{x} \mapsto \frac{1}{n} \sum_{j=1}^n h_n(\mathbf{x}, \mathbf{y}_j) \quad \text{and} \quad \xi_n : \mathbf{y} \mapsto \frac{1}{n} \sum_{j=1}^n h_n(\mathbf{x}_i, \mathbf{y}) \quad (19)$$

From Eq. (18), we get that $\mathbf{P}_{\varepsilon, \tau}^{i,j} = \frac{1}{n^2} h(\mathbf{x}_i, \mathbf{y}_j)$, so reminding that $\mathbf{a} = \mathbf{P}_{\varepsilon, \tau} \mathbf{1}_n$ and $\mathbf{b} = \mathbf{P}_{\varepsilon, \tau}^\top \mathbf{1}_n$, one has $n a_i = \eta_n(X_i)$ and $n b_i = \xi_n(Y_i)$. We now show that almost surely, $\eta_n \rightarrow \eta$ and $\xi_n \rightarrow \xi$ pointwise, which implies the desired result that, almost surely, $n a_i \rightarrow \eta(X_i)$ and $n b_i \rightarrow \xi(Y_i)$.

Almost surely, $\hat{\mu}_n \rightarrow \mu$ and $\hat{\nu}_n \rightarrow \nu$, so using (Séjourné et al., 2021, Proposition 10), $f_n^* \rightarrow f^*$ and $g_n^* \rightarrow g^*$ in sup-norm. Since $f_n^* \rightarrow f^*$ on \mathcal{X} and $g_n^* \rightarrow g^*$ on \mathcal{Y} in sup-norm, we can show that $h_n \rightarrow h$ in sup-norm on $\mathcal{X} \times \mathcal{Y}$. Indeed, for

$(\mathbf{x}, \mathbf{y}) \in (\mathcal{X} \times \mathcal{Y})$, one has:

$$\begin{aligned}
 & |h_n(\mathbf{x}, \mathbf{y}) - h(\mathbf{x}, \mathbf{y})| \\
 &= \left| \exp\left(\frac{f_n^*(\mathbf{x}) + g_n^*(\mathbf{y}) - c(\mathbf{x}, \mathbf{y})}{\varepsilon}\right) - \exp\left(\frac{f^*(\mathbf{x}) + g^*(\mathbf{y}) - c(\mathbf{x}, \mathbf{y})}{\varepsilon}\right) \right| \\
 &= \exp\left(\frac{c(\mathbf{x}, \mathbf{y})}{\varepsilon}\right) \left| \exp\left(\frac{f_n^*(\mathbf{x}) + g_n^*(\mathbf{y})}{\varepsilon}\right) - \exp\left(\frac{f^*(\mathbf{x}) + g^*(\mathbf{y})}{\varepsilon}\right) \right| \\
 &\leq M_{c,\varepsilon} \left| \exp\left(\frac{f_n^*(\mathbf{x}) + g_n^*(\mathbf{y})}{\varepsilon}\right) - \exp\left(\frac{f^*(\mathbf{x}) + g^*(\mathbf{y})}{\varepsilon}\right) \right|
 \end{aligned} \tag{20}$$

with $M_{c,\varepsilon} = \sup_{(\mathbf{x}, \mathbf{y}) \in \mathcal{X} \times \mathcal{Y}} \exp\left(\frac{c(\mathbf{x}, \mathbf{y})}{\varepsilon}\right) < +\infty$, since $(\mathbf{x}, \mathbf{y}) \mapsto \exp\left(\frac{c(\mathbf{x}, \mathbf{y})}{\varepsilon}\right)$ is continuous on the compact $\mathcal{X} \times \mathcal{Y}$, as c is continuous. Afterwards,

$$\begin{aligned}
 & \left| \exp\left(\frac{f_n^*(\mathbf{x}) + g_n^*(\mathbf{y})}{\varepsilon}\right) - \exp\left(\frac{f^*(\mathbf{x}) + g^*(\mathbf{y})}{\varepsilon}\right) \right| \\
 &\leq \left| \exp\left(\frac{f_n^*(\mathbf{x})}{\varepsilon}\right) \exp\left(\frac{g_n^*(\mathbf{y})}{\varepsilon}\right) - \exp\left(\frac{f_n^*(\mathbf{x})}{\varepsilon}\right) \exp\left(\frac{g^*(\mathbf{y})}{\varepsilon}\right) \right| \\
 &+ \left| \exp\left(\frac{f_n^*(\mathbf{x})}{\varepsilon}\right) \exp\left(\frac{g^*(\mathbf{y})}{\varepsilon}\right) - \exp\left(\frac{f^*(\mathbf{x})}{\varepsilon}\right) \exp\left(\frac{g^*(\mathbf{y})}{\varepsilon}\right) \right|
 \end{aligned} \tag{21}$$

For the first term, one has:

$$\begin{aligned}
 & \left| \exp\left(\frac{f_n^*(\mathbf{x})}{\varepsilon}\right) \exp\left(\frac{g_n^*(\mathbf{y})}{\varepsilon}\right) - \exp\left(\frac{f_n^*(\mathbf{x})}{\varepsilon}\right) \exp\left(\frac{g^*(\mathbf{y})}{\varepsilon}\right) \right| \\
 &= \exp\left(\frac{f_n^*(\mathbf{x})}{\varepsilon}\right) \left| \exp\left(\frac{g_n^*(\mathbf{y})}{\varepsilon}\right) - \exp\left(\frac{g^*(\mathbf{y})}{\varepsilon}\right) \right| \\
 &\leq \exp\left(\frac{\|f_n^*\|_\infty}{\varepsilon}\right) \left| \exp\left(\frac{g_n^*(\mathbf{y})}{\varepsilon}\right) - \exp\left(\frac{g^*(\mathbf{y})}{\varepsilon}\right) \right|
 \end{aligned} \tag{22}$$

First, we can bound uniformly $\exp(\|f_n^*\|_\infty/\varepsilon)$ since f_n converges in sup-norm, so $(\|f_n^*\|_\infty)_{n \geq 0}$ is bounded. Then, since g_n^* converges in sup-norm, it is uniformly bounded, and since g^* is continuous on the compact \mathcal{X} , it is bounded. Therefore, we can find a compact $K \subset \mathbb{R}$ s.t. $g^*(\mathcal{X}) \subset K$ and for each n , $g_n^*(\mathcal{X}) \subset K$. Then, applying the mean value theorem to the C_1 function $\mathbf{x} \mapsto \exp(\mathbf{x}/\varepsilon)$ on K , we can bound:

$$\left| \exp\left(\frac{g_n^*(\mathbf{y})}{\varepsilon}\right) - \exp\left(\frac{g^*(\mathbf{y})}{\varepsilon}\right) \right| \leq \sup_{\mathbf{z} \in K} \frac{1}{\varepsilon} \exp\left(\frac{1}{\varepsilon} \mathbf{z}\right) |g_n^*(\mathbf{y}) - g^*(\mathbf{y})| \tag{23}$$

This yields the existence of a constant $M_1 > 0$ s.t.

$$\left| \exp\left(\frac{f_n^*(\mathbf{x})}{\varepsilon}\right) \exp\left(\frac{g_n^*(\mathbf{y})}{\varepsilon}\right) - \exp\left(\frac{f_n^*(\mathbf{x})}{\varepsilon}\right) \exp\left(\frac{g^*(\mathbf{y})}{\varepsilon}\right) \right| \leq M_1 \|g_n^* - g^*\|_\infty \tag{24}$$

Using the same strategy, we get the existence of a constant $M_2 > 0$ s.t.

$$\left| \exp\left(\frac{f_n^*(\mathbf{x})}{\varepsilon}\right) \exp\left(\frac{g^*(\mathbf{y})}{\varepsilon}\right) - \exp\left(\frac{f^*(\mathbf{x})}{\varepsilon}\right) \exp\left(\frac{g^*(\mathbf{y})}{\varepsilon}\right) \right| \leq M_2 \|f_n^* - f^*\|_\infty \tag{25}$$

Combining (24) and (25) with (20), we get that:

$$|h_n(\mathbf{x}) - h(\mathbf{x})| \leq M_{c,\varepsilon} (M_1 \|g_n^* - g^*\|_\infty + M_2 \|f_n^* - f^*\|_\infty) \tag{26}$$

from which we deduce that $h_n \rightarrow h$ in sup-norm, from the convergence of $f_n \rightarrow f$ and $g_n \rightarrow g$ in sup-norm.

Now, we can show the pointwise convergence of $\hat{\eta}_n$. For any $\mathbf{x} \in \mathcal{X}$, one has:

$$\begin{aligned}
 & |\hat{\eta}_n(\mathbf{x}) - \eta(\mathbf{x})| \\
 &= \left| \int h_n(\mathbf{x}, \mathbf{y}) d\hat{\nu}_n(\mathbf{y}) - \int h(\mathbf{x}, \mathbf{y}) d\nu(\mathbf{y}) \right| \\
 &\leq \left| \int h_n(\mathbf{x}, \mathbf{y}) d\hat{\nu}_n(\mathbf{y}) - \int h(\mathbf{x}, \mathbf{y}) d\hat{\nu}_n(\mathbf{y}) \right| + \left| \int h(\mathbf{x}, \mathbf{y}) d\hat{\nu}_n(\mathbf{y}) - \int h(\mathbf{x}, \mathbf{y}) d\nu(\mathbf{y}) \right| \\
 &\leq \int \|h_n - h\|_\infty d\hat{\nu}_n(\mathbf{y}) + \left| \int h(\mathbf{x}, \mathbf{y}) d\hat{\nu}_n(\mathbf{y}) - \int h(\mathbf{x}, \mathbf{y}) d\nu(\mathbf{y}) \right| \\
 &= \|h_n - h\|_\infty + \left| \int h(\mathbf{x}, \mathbf{y}) d\hat{\nu}_n(\mathbf{y}) - \int h(\mathbf{x}, \mathbf{y}) d\nu(\mathbf{y}) \right|
 \end{aligned} \tag{27}$$

Therefore, it almost surely holds that $\hat{\eta}_n(\mathbf{x}) \rightarrow \eta(\mathbf{x})$. Indeed, $\|h_n - h\|_\infty \rightarrow 0$ since we have shown that $h_n \rightarrow h$ in sup-norm. Then, h is continuous on the compact $\mathcal{X} \times \mathcal{Y}$, so it is bounded, so since $\mu_n \rightarrow \mu$, we get $\int h d\hat{\nu}_n \rightarrow \int h d\nu$. Next, we show similarly that, almost surely, $\xi_n \rightarrow \xi$ pointwise. \square

B. Metrics

We start with introducing general metrics in § B.1, some of which will be used in the metrics introduced in the context of experiments on single-cell data in § B.2.

B.1. General metrics

In the following, we discuss a way how to classify predictions in a generative model. We start with the setting where each mapped sample is to be assigned to a category based on labelled data in the target distribution. We then continue with the case where there are also labels for samples in the source distribution, and this way define a classifier f_{class} between labels in the source distribution and labels in the target distribution. Building upon this, we assign the classifier f_{class} an uncertainty score for each prediction. Finally, we define a calibration score assessing the quality of a given uncertainty score.

Turning a generative model into a classifier In the following, consider a finite set of samples in the target domain $\mathbf{y}_1, \dots, \mathbf{y}_M \in \mathcal{Y}$. Assume $\{\mathbf{y}_m\}_{m=1}^M$ allows for a partition $\{\mathbf{y}_m\}_{m=1}^M = \sqcup_{k \in K} \mathcal{T}_k$. Hence, each sample belongs to exactly one class, which we interchangeably refer to as the sample being labelled. Let $T : \mathcal{X} \rightarrow \mathcal{Y}$ be a map (deterministic or stochastic), and let $f_{1\text{-NN}} : \mathcal{Y} \rightarrow \{\mathcal{T}_k\}_{k=1}^K$ be the 1-nearest neighbor classifier. We obtain a map g from \mathcal{X} to $\{\mathcal{T}_k\}_{k=1}^K$ by the concatenation of $f_{1\text{-NN}}$ and T . This map g proves useful in settings when mapped cells are to be categorized, e.g. to assign mapped cells to a cell type.

A metric to assess the accuracy of a generative model In the following, assume that the set of samples in the source domain $\mathbf{x}_1, \dots, \mathbf{x}_N$ allows for a partition $\{\mathbf{x}_n\}_{n=1}^N = \sqcup_{k \in K} \mathcal{S}_k$. Note that the number of elements in the partition of both the source and the target domain is set to K . We want to construct a classifier f_{class} assigning each category in the source distribution $\{\mathcal{S}_k\}_{k=1}^K$ probabilistically to a category in the target distribution $\{\mathcal{T}_k\}_{k=1}^K$. Define $f_{\text{class}} : \{\mathcal{S}_k\}_{k=1}^K \rightarrow \mathbb{N}^K$ via $(f_{\text{class}}(\mathcal{S}_k))_j = \sum_{\mathbf{x}_n \in \mathcal{S}_k} 1_{\{g(\mathbf{x}_n) = \mathcal{T}_j\}}$ where $g : \mathcal{X} \rightarrow \{\mathcal{T}_k\}_{k=1}^K$ was defined above.

Assume that there exists a known one-to-one match between elements in $\{\mathcal{S}_k\}_{k=1}^K$ and elements in $\{\mathcal{T}_k\}_{k=1}^K$. Then we can define a confusion matrix \mathcal{A} with entries $\mathcal{A}_{ij} := \sum_{\mathbf{x}_n \in \mathcal{T}_i} 1_{\{g(\mathbf{x}_n) = \mathcal{S}_j\}}$. In the context of entropic OT the confusion matrix is element-wise defined as

$$\mathcal{A}_{ij} := \sum_{\mathbf{x}_n \in \mathcal{T}_i} 1_{\{f_{1\text{-NN}}(T(\mathbf{x}_n)) = \mathcal{S}_j\}} \tag{28}$$

This way we obtain an accuracy score of the classifier f_{class} mapping a partition of one set of samples to a partition of another set of samples.

Calibration score To assess the meaningfulness of an uncertainty score, we introduce the following calibration score. Assume we have a classifier which yields predictions along with uncertainty estimations. Let $\mathbf{u} \in \mathbb{R}^K$ be a vector containing an uncertainty estimation for each element in $\{\mathcal{S}_k\}_{k=1}^K$. Moreover, let $\mathbf{a} \in \mathbb{R}^K$ be a vector containing the accuracy for each element in $\{\mathcal{S}_k\}_{k=1}^K$. We then define our calibration score to be the Spearman rank correlation coefficient between u and $\mathbf{1}_K - a$, where $\mathbf{1}_K$ denotes the K -dimensional vector containing 1 in every entry. In effect, the calibration score is close to 1 if the model assigns high uncertainty to wrong predictions and low uncertainty to true predictions, while the calibration score is close to -1 if the model assigns high uncertainty to correct predictions and low uncertainty to wrong predictions.

In the following, we consider a stochastic map T . Let $\mathbf{y}_1, \dots, \mathbf{y}_L \sim \pi_\theta(\cdot|\mathbf{x})$ obtained from T . To obtain a calibration score for f_{class} we estimate a statistic $V(\pi_\theta(\cdot|\mathbf{x}))$ from the samples $\mathbf{y}_1, \dots, \mathbf{y}_L$, reflecting an estimation of uncertainty. Then, we let the uncertainty of the prediction of f_{class} for category \mathcal{S}_i be the mean uncertainty statistic, i.e. $\sum_{\mathbf{x} \in \mathcal{S}_i} \frac{V(\pi_\theta(\cdot|\mathbf{x}))}{|\mathcal{S}_i|}$. In effect, for each prediction $f_{\text{class}}(\mathcal{S}_i)$ we get the uncertainty score

$$u_i = \sum_{\mathbf{x} \in \mathcal{S}_i} \frac{V(\pi_\theta(\cdot|\mathbf{x}))}{|\mathcal{S}_i|}. \quad (29)$$

Assessing the uncertainty with the *cos-var* metric Gayoso et al. (2022) introduce a statistic to assess the uncertainty of deep generative RNA velocity methods from samples of the posterior distribution, which we adapt to the OT paradigm to obtain

$$\text{cos-var}(\pi_\theta(\cdot|\mathbf{x})) = \text{Var}_{Y \sim \pi_\theta(\cdot|\mathbf{x})}[\text{cos-sim}(Y, \mathbb{E}_{Y \sim \pi_\theta(\cdot|\mathbf{x})}[Y])], \quad (30)$$

where *cos-sim* denotes the cosine similarity. We refer to this metric as *cos-var*, as it computes the variance of the cosine similarity of samples following the conditional distribution and the conditional mean. We use 30 samples from the conditional distribution to compute this metric.

B.2. Single-cell specific metrics

Cell type scores As in most single-cell tasks there is no ground truth of matches between cells, we rely on labels of clusters of the data, i.e. on cell types. We then assess the accuracy of a generative model by considering the accuracy of the corresponding classifier f_{class} as described above. The correct matches between classes have to be considered task-specifically. In the following, we discuss the choice of the labels $\{\mathcal{S}_k\}_{k=1}^K$ and $\{\mathcal{T}_k\}_{k=1}^K$ for perturbation prediction.

Each drug was applied to cells belonging to three different cell types/cell lines, namely A549, K562, and MCF7. Hence, we can define $\{\mathcal{S}_k\}_{k=1}^K = \{\mathcal{T}_k\}_{k=1}^K = \{A549, K562, MCF7\}$ as for each perturbed cell we know the cell type at the time of injecting the drug.

FOSCTTM score In the following, we consider a setting where the true match between *samples* is known. The FOSCTTM score ("Fraction of Samples Closer than True Match") measures the fraction of cells which are closer to the true match than the predicted cell. Hence, a random match has a FOSCTTM score of 0.5, while a perfect match has a FOSCTTM score of 0.0. In the following we only consider discrete distributions. To define the FOSCTTM score for a map $T : \mathcal{X} \rightarrow \mathcal{Y}$, let $\mathbf{x}_1, \dots, \mathbf{x}_K \in \mathcal{X}$ be samples from the source distribution and $\mathbf{y}_1, \dots, \mathbf{y}_K \in \mathcal{Y}$ be samples from the target distribution, such that \mathbf{x}_k and \mathbf{y}_k form a true match. Moreover, let $\hat{\mathbf{y}}_k = T(\mathbf{x}_k)$. Let

$$p_j = \frac{\sum_{k \in K} \mathbf{1}_{\|\mathbf{y}_k - \hat{\mathbf{y}}_j\|_2 \leq \|\mathbf{y}_j - \hat{\mathbf{y}}_j\|_2}}{|K|} \quad (31)$$

and

$$q_j = \frac{\sum_{k \in K} \mathbf{1}_{\|\mathbf{y}_j - \hat{\mathbf{y}}_k\|_2 \leq \|\mathbf{y}_j - \hat{\mathbf{y}}_j\|_2}}{|K|} \quad (32)$$

Then, the FOSCTTM score between the predicted target $\{\hat{\mathbf{y}}_k\}_{k \in K}$ and the target $\{\mathbf{y}_k\}_{k \in K}$ is obtained as

$$\text{FOSCTMM}(\{\hat{\mathbf{y}}_k\}_{k \in K}, \{\mathbf{y}_k\}_{k \in K}) = \sum_{k \in K} \frac{p_j + q_j}{2}. \quad (33)$$

C. Datasets

C.1. Gushchin et al. (2023)’s benchmark datasets

We follow the notebook in https://github.com/ngushchin/EntropicOTBenchmark/blob/main/notebooks/mixtures_benchmark_visualization_eot.ipynb, which allows to download the data when instantiating the samplers by setting `download=True` in the function `get_guassain_mixture_benchmark_sampler()`.

C.2. Pancreas single-cell dataset

The dataset of the developing mouse pancreas was published in Bastidas-Ponce et al. (2019) and can be downloaded following the guidelines on <https://www.ncbi.nlm.nih.gov/geo/query/acc.cgi?acc=GSE132188>. The full dataset contains measurements of embryonic days 12.5, 13.5, 14.5, and 15.5, while we only consider time points 14.5 and 15.5.

We filter the dataset such that we only keep cells belonging to the cell types of the endocrine branch to ensure that learnt transitions are biologically plausible. Moreover, cells annotated as *Ngn3 high cycling* were removed due to its unknown stage in the developmental process (Bastidas-Ponce et al., 2019). The removal is justified by the small number of cells belonging to this cell type and its outlying position in gene expression space. Experiments were performed on 30-dimensional PCA space of log-transformed gene expression counts.

C.3. Drug perturbation single-cell dataset

The dataset was published in (Srivatsan et al., 2020). We download the dataset following the instructions detailed on <https://github.com/bunnech/cellot/tree/main>.

For all analyses (figure 5.1) we computed PCA embeddings on the filtered dataset including the control cells and the corresponding drug only. This ensures the capturing of relevant distributional shifts and hence prevents the model from near-constant predictions as the effect of numerous drugs is weak.

The drugs in figure 5.1 were chosen as in Hetzel et al. (2022).

C.4. Human bone marrow single-cell dataset for modality translation

This dataset contains paired measurements of single-cell RNA-seq readouts and single-nucleus ATAC-seq measurements (Luecken et al., 2021). This means that we have a ground truth one-to-one matching for each cell. We use the processed data provided in moscot (Klein et al., 2023), which can be downloaded following the instructions on https://moscot.readthedocs.io/en/latest/genapi/moscot.datasets.bone_marrow.html#moscot.datasets.bone_marrow. This version of the dataset additionally contains a shared embedding for both the RNA and the ATAC data, which we use in the fused term. This embedding was created using a variational autoencoder (scVI (Lopez et al., 2018b)) by integrating the RNA counts of the gene expression dataset and gene activity (Stuart et al., 2021) derived from the ATAC data, a commonly used approximation for gene expression estimation from ATAC data (Heumos et al., 2023).

In RNA space we use the PCA embedding (the dimension of which is detailed in the corresponding experiments), while the embedding used in ATAC space is the given LSI (latent semantic indexing) embedding, followed by a feature-wise L2-normalization as proposed in Demetci et al. (2022). The legend for the cell type labels is given in Fig. 23.

D. Additional information and results for experiments

If not stated otherwise, the GENOT model configuration follows the setup described in appendix F.

D.1. 1d simulated data

While figure 3 shows results for $\tau = \tau_1 = \tau_2 = 0.98$, figure 11 visualizes the influence of τ . While $\tau = 1.0$ corresponds to the fully balanced case, setting $\tau = 0.97$ results in a complete discardment of one mode in the target distribution. The ground truth is computed with a discrete entropy-regularized OT solver (Cuturi et al., 2022).

D.2. GENOT-L benchmarks

Entropic OT benchmark by Gushchin et al. (2023) We assess the performance of GENOT-L following the benchmark in Gushchin et al. (2023). While the results reported in Gushchin et al. (2023) are the best ones across different configurations of hyperparameters for certain models, we choose *a single hyperparameter configuration* across all dimensions and entropy regularisation parameters. In particular, GENOT is trained for 100,000 iterations and the learning rate is set to 10^{-5} . The dimension of the layers in the vector field is set to 1024, and the entropy regularization parameter is set according to the task (i.e. 0.1, 1.0 or 10.0.). The batch size is set to 2048, and its influence is further studied in figure 9. The number of layers per block is set to 3, and the embedding dimension of the time, condition, and noise is set to 1,024. All remaining parameters are chosen as described in appendix F.

Following Gushchin et al. (2023), Tab. 2 reports the Bures-Wasserstein Unexplained Variance Percentage ($\text{BW}_2^2\text{-UVP}$) between the marginal distributions $p_{2\#}\pi_\theta$ and ν defined as

$$\text{BW}_2^2\text{-UVP}(p_{2\#}\pi_\theta, \nu) = \frac{100\%}{\frac{1}{2} \text{Var}(\nu)} \text{BW}_2^2(p_{2\#}\pi_\theta, \nu) \quad (34)$$

where $\text{BW}_2^2(p_{2\#}\pi_\theta, \pi_2^*)$ is the Bures-Wasserstein metric between the Gaussian approximations of the distributions $p_{2\#}\pi_\theta$ and ν :

$$\text{BW}_2^2(p_{2\#}\pi_\theta, \nu) = W_2^2(\mathcal{N}(m_\nu, \Sigma_\nu), \mathcal{N}(m_{p_{2\#}\pi_\theta}, \Sigma_{p_{2\#}\pi_\theta})). \quad (35)$$

Here, W_2^2 denotes the Wasserstein-2 distance, and for any measure γ , m_γ denotes its mean and Σ_γ its covariance. Tab. 3 displays the conditional Bures-Wasserstein Unexplained Variance Percentage (cBW-UVP), which is the integration of the Bures-Wasserstein distances of the estimated and the true conditional distributions:

$$\text{cBW}_2^2\text{-UVP}(\pi_\theta, \pi_\varepsilon^*) = \frac{100\%}{\frac{1}{2} \text{Var}(\nu)} \int_{\mathcal{X}} \text{BW}_2^2(\pi_\theta(\cdot|\mathbf{x}), \pi_\varepsilon^*(\cdot|\mathbf{x})) d\mu(\mathbf{x}). \quad (36)$$

Hence, $\text{BW}_2^2\text{-UVP}(p_{2\#}\pi_\theta, \nu)$ measures the fitting property of the push-forward distribution while $\text{cBW}_2^2\text{-UVP}(\pi_\theta, \pi_\varepsilon^*)$ measures the fitting property of the joint distribution. Hence, $\text{BW}_2^2\text{-UVP}(p_{2\#}\pi_\theta, \nu)$ measures the fitting property of the push-forward distribution while $\text{cBW}_2^2\text{-UVP}(\pi_\theta, \pi_\varepsilon^*)$ measures the fitting property of the joint distribution.

The values for the competing methods are taken from the original manuscript Gushchin et al. (2023). Competing methods are Seguy et al. (2017) (LSOT), Daniels et al. (2021) (SCONES), Korotin et al. (2022) (NOT), Mokrov et al. (2023) (EgNOT), Gushchin et al. (2022) (ENOT), Vargas et al. (2021) (MLE-SB), De Bortoli et al. (2021) (DiffSB), Chen et al. (2021) (FB-SDE-A, FB-SDE-J).

To make the results of the benchmark more interpretable, we rank the methods for each experimental setup. If multiple methods yield the same result, we assign the methods the mean of the ranks. Tab. 1 reports the average rank across the twelve different experimental setups.

Ablation study of GENOT A natural way to extend the GENOT algorithm is to sample $k > 1$ instances from the conditional distribution. Alg. 2 describes this procedure in lines 8 to 11, resulting only in an additional sum in the loss in line 12. As for each condition X_i we then have multiple samples $\{Z_{i_l}\}_{l=1}^k$ and $\{Y_{i_l}\}_{l=1}^k$ (in the unbalanced case k depends on i), we can then couple the noise samples with the samples from the conditional distribution using a discrete Sinkhorn solver (note that the noise and the conditional distribution always live in the same space). This corresponds to using the approach introduced in Tong et al. (2023b); Pooladian et al. (2023) for each single conditional generator $T_\theta(\cdot|\mathbf{x})$. We study this natural extension of the GENOT model in Fig 10. While in a few cases this extensions helps, in the majority of experiments using $k > 1$ decreases the performance.

GENOT-L for trajectory inference Discrete optimal transport is an established method for trajectory inference in single-cell genomics (Schiebinger et al., 2019). Due to the ever increasing size of these datasets (Haniffa et al., 2021), neural OT solvers are of particular interest and deterministic Monge map estimators have been successfully applied to millions of cells (He et al., 2023).

Algorithm 2 U-GENOT with stratified sampling of the discrete conditionals. Skip teal steps for GENOT.

- 1: **Require parameters:** Batch size n , number of (per \mathbf{x}) conditional sample k , entropic regularization ε , **unbalancedness parameter** τ , discrete solver $\text{Solver}_{\varepsilon, \tau}$.
- 2: **Require network:** Time-dependent conditional velocity field $v_{t, \theta}(\cdot) : \mathbb{R}^q \times \mathbb{R}^p \rightarrow \mathbb{R}^q$, **re-weighting functions** $\eta_{\theta} : \mathbb{R}^p \rightarrow \mathbb{R}$, $\xi_{\theta} : \mathbb{R}^q \rightarrow \mathbb{R}$.
- 3: **for** $t = 1, \dots, T_{\text{iter}}$ **do**
- 4: $X_1, \dots, X_n \sim \mu$ and $Y_1, \dots, Y_n \sim \nu$.
- 5: $\mathbf{P}_{\varepsilon, \tau} \leftarrow \text{Solver}_{\varepsilon, \tau}((X_i)_{i=1}^n, (Y_i)_{i=1}^n) \in \mathbb{R}_+^{n \times n}$.
- 6: $\mathbf{a} \leftarrow \mathbf{P}_{\varepsilon, \tau} \mathbf{1}_n$ and $\mathbf{b} \leftarrow \mathbf{P}_{\varepsilon, \tau}^{\top} \mathbf{1}_n$.
- 7: **Sample** $i_1, \dots, i_n \sim \mathbf{a}$ and set $(X_1, \dots, X_n) \leftarrow (X_{i_1}, \dots, X_{i_n})$.
- 8: **for** $i = 1, \dots, n$ **do**
- 9: **Sample** $i_1, \dots, i_k \sim \mathbf{P}_{\varepsilon, \tau}[i, :]$.
- 10: **Sample** noise vectors $Z_{i,1}, \dots, Z_{i,k} \sim \rho$ and time-steps $t_{i,1}, \dots, t_{i,k} \sim \mathcal{U}([0, 1])$.
- 11: **end for**
- 12: $\mathcal{L}(\theta) \leftarrow \frac{1}{n} \sum_{i=1}^n \frac{1}{k} \sum_{l=1}^k \|v_{t, \theta}([Z_{i,l}, Y_{i,l}]_t | X_i) - (Y_i - Z_{i,l})\|_2^2 + \frac{1}{n} \sum_{i=1}^n (\eta_{\theta}(X_i) - n\mathbf{a}_k)^2 + (\xi_{\theta}(Y_i) - n\mathbf{b}_k)^2$.
- 13: $\theta \leftarrow \text{Update}(\theta, \nabla \mathcal{L}(\theta))$.
- 14: **end for**

Model	$\varepsilon = 0.1$				$\varepsilon = 1$				$\varepsilon = 10$			
	2	16	64	128	2	16	64	128	2	16	64	128
LSOT	-(9.5)	-(9.5)	-(9.5)	-(9.5)	-(10)	-(10)	-(10)	-(10)	-(8.5)	-(8.5)	-(8.5)	-(8.5)
SCONES	-(9.5)	-(9.5)	-(9.5)	-(9.5)	1.06 (9)	4.24 (9)	6.67 (8)	11.54 (8)	1.11 (5)	2.98 (6)	1.33 (3)	7.89 (4)
NOT	0.016 (3)	0.63 (5)	1.53 (5)	2.62 (5)	0.08 (3)	1.13 (8)	1.62 (7)	2.62 (7)	0.225 (4)	2.603 (5)	1.872 (4)	6.12 (3)
EgNOT	0.09 (5)	0.31 (4)	0.88 (3)	0.22 (1)	0.46 (6)	0.3 (4)	0.85 (4)	0.12 (1)	0.077 (1)	0.02 (1.5)	0.15 (1)	0.23 (1)
ENOT	0.2 (6)	2.9 (8)	1.8 (6)	1.4 (3)	0.22 (5)	0.4 (5)	7.8 (9)	29 (9)	1.2 (6)	2 (4)	18.9 (6)	28 (6)
MLE-SB	0.01 (2)	0.14 (3)	0.97 (4)	2.08 (4)	0.005 (1)	0.09 (2)	0.56 (2)	1.46 (5)	0.01 (2)	1.02 (3)	6.65 (5)	23.4 (5)
DiffSB	2.88 (8)	2.81 (7)	153.22 (8)	232.67 (8)	0.87 (8)	0.99 (7)	1.12 (5)	1.56 (6)	-(8.5)	-(8.5)	-(8.5)	-(8.5)
FB-SDE-A	2.37 (7)	2.55 (6)	68.19 (7)	27.11 (7)	0.6 (7)	0.63 (6)	0.65 (3)	0.71 (4)	-(8.5)	-(8.5)	-(8.5)	-(8.5)
FB-SDE-J	0.03 (4)	0.05 (2)	0.25 (2)	2.96 (6)	0.07 (2)	0.13 (3)	1.52 (6)	0.48 (3)	-(8.5)	-(8.5)	-(8.5)	-(8.5)
GENOT	0.003 (1)	0.015 (1)	0.13 (1)	0.33 (2)	0.085 (4)	0.06 (1)	0.08 (1)	0.18 (2)	0.10 (3)	0.02 (1.5)	0.30 (2)	0.47 (2)

Table 2. BW_2^2 -UVP (equation (34)) between π_2 and $p_2 \# \pi_{\theta}$ between the distributions defined in Gushchin et al. (2023), with numbers in parantheses denoting the rank within the experimental configuration defined by the dimension of the space and the entropy regularization parameter ε .

Obtaining samples from the conditional distribution allows for an assessment of the uncertainty of the trajectory of a cell. We use the metric $\text{Var}_{Y \sim \pi_{\theta}(\cdot | \mathbf{x})}[\text{cos-sim}(Y, \mathbb{E}_{Y \sim \pi_{\theta}(\cdot | \mathbf{x})}[Y])]$ suggested in Gayoso et al. (2022) for generative RNA velocity models (appendix B.1). Therefore, we use 30 samples from the conditional distribution.

Fig. 12 visualizes the pancreatic endocrinogenesis dataset (C.2) according to source (embryonic day 14.5) and target distribution (15.5) as well as according to cell type. To quantitatively confirm the visual results from Fig. 4, we aggregate the uncertainty to cell type level. Indeed, we observe a higher uncertainty in cells which have not committed to a certain lineage (Ngn3 low, Ngn3 High early, Ngn3 High late), while more mature cell types indicate lower variances.

A cell is expected to have an uncertain trajectory when it can still develop into different cell lineages. In contrast, cells are expected to have a less uncertain trajectory when their descending population is homogeneous or they belong to a terminal cell state, and hence have committed to a certain lineage.

GENOT-L produces meaningful uncertainty assessments as can be seen from Fig. 4 and Fig. 12. Indeed, the Ngn3 low EP population and the Ngn3 high EP populations have a higher uncertainty than later cell types. The uncertainty is particularly high for Ngn3 high EP late cells, a state where cells commit to a fate towards alpha, beta, delta, or epsilon cells (Bastidas-Ponce et al., 2019).

We now focus on the conditional distributions of cells from the Ngn3 low population, i.e. the least mature cell population in the dataset. Fig. 13 shows more examples of selecting one Ngn3 low cell and generating 30 samples from its conditional distribution as displayed in Fig 4. It is important to note that the UMAP has to be recomputed to include the generated

Entropic (Gromov) Wasserstein Flow Matching with GENOT

Model	$\epsilon = 0.1$				$\epsilon = 1$				$\epsilon = 10$			
	2	16	64	128	2	16	64	128	2	16	64	128
LSOT	-(9.5)	-(9.5)	(9.5)	-(9.5)	-(10)	-(10)	-(10)	-(10)	-(8.5)	-(8.5)	-(8.5)	-(8.5)
SCONES	-(9.5)	-(9.5)	(9.5)	-(9.5)	34.88 (8)	71.34 (8)	59.12 (7)	136.44 (7)	32.9 (6)	50.84 (6)	60.44 (6)	52.11 (6)
NOT	1.94 (2)	13.67 (2)	11.74 (1)	11.4 (1)	4.77 (3)	23.27 (4)	41.75 (5)	26.56 (3)	2.86 (3)	4.57 (5)	3.41 (3)	6.56 (3)
EgNOT	129.8 (8)	75.2 (7)	60.4 (5)	43.2 (5)	80.4 (9)	74.4 (9)	63.8 (8)	53.2 (5)	4.14 (5)	2.64 (4)	2.36 (2)	1.31 (2)
ENOT	3.64 (3)	22 (4)	13.6 (2)	12.6 (2)	1.04 (1)	9.4 (3)	21.6 (3)	48 (4)	1.4 (1)	2.4 (3)	19.6 (5)	30 (5)
MLE-SB	4.57 (4)	16.12 (3)	16.1 (4)	17.81 (3)	4.13 (2)	9.08 (1)	18.05 (2)	15.226 (2)	1.61 (2)	1.27 (1)	3.9 (4)	12.9 (4)
DiffSB	73.54 (6)	59.7 (6)	1386.4 (8)	1683.6 (8)	33.76 (7)	70.86 (7)	53.42 (6)	156.46 (8)	-(8.5)	-(8.5)	-(8.5)	-(8.5)
FB-SDE-A	86.4 (7)	53.2 (5)	1156.82 (7)	1566.44 (7)	30.62 (6)	63.48 (5)	34.84 (4)	131.72 (6)	-(8.5)	-(8.5)	-(8.5)	-(8.5)
FB-SDE-J	51.34 (5)	89.16 (8)	119.32 (6)	173.96 (6)	29.34 (5)	69.2 (6)	155.14 (9)	177.52 (9)	-(8.5)	-(8.5)	-(8.5)	-(8.5)
Independent	166.0	152.0	126.0	110.0	86.0	80.0	72.0	60.0	4.2	2.52	2.26	2.4
GENOT	0.46 (1)	0.91 (1)	14.48 (3)	28.52 (4)	7.43 (4)	9.10 (2)	8.61 (1)	6.76 (1)	3.24 (4)	1.97 (2)	0.91 (1)	1.03 (1)

Table 3. cBW_2^2 -UVP (34) between π_ϵ^* and π_θ between the distributions defined in Gushchin et al. (2023), with numbers in parantheses denoting the rank within the experimental configuration defined by the dimension of the space and the entropy regularization parameter ϵ .

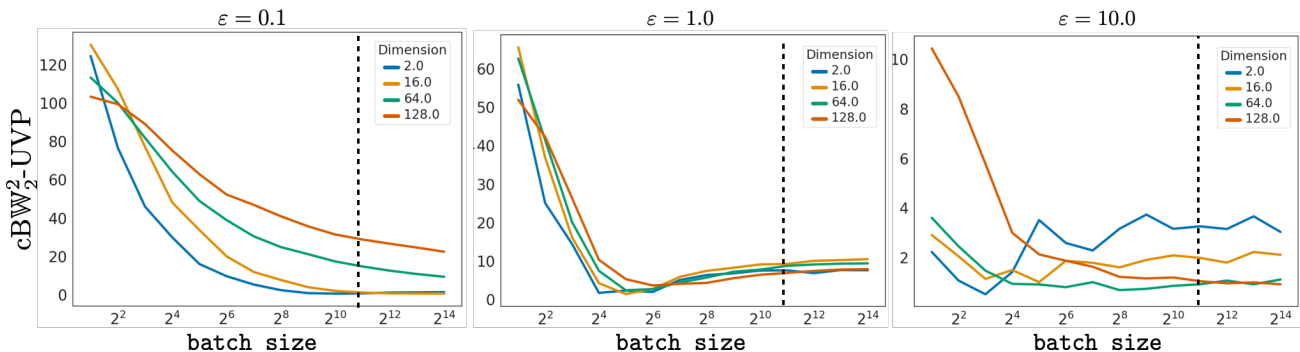


Figure 9. cBW_2^2 -UVP (34) between π_ϵ^* and π_θ between the distributions defined in Gushchin et al. (2023) depending on the batch size. The dotted line corresponds to batch size 2048 and hence displays the values reported in Tab. 3.

samples and hence the UMAPs change slightly. The three instances in Fig.13 support the hypothesis that the conditional distribution follows the data manifold when using the geodesic cost (here we assume that the UMAP represents the manifold well). In contrast, choosing the squared Euclidean distance results in samples of the conditional distribution being either very close on the UMAP or very far away, while the intermediate stage (i.e. Ngn3 High late) is skipped. Biologically, this result is not plausible as all cells are known to evolve from Ngn3 Low EP cells to Ngn3 High EP cells, before they finally commit to a lineage (towards alpha, beta, delta, or epsilon cells). It is important to note that both GENOT-L models are trained with the same entropy regularization parameter $\epsilon = 0.01$.

Based on the examples, we hence hypothesize that when using the squared Euclidean cost, generated cells in the terminal cell states (alpha, beta, delta, epsilon) are much more likely to be derived from Ngn3 low EP cells than Ngn3 High EP cells (in the following we focus on Ngn3 High Late cells and neglect Ngn3 High EP early cells as their number is very low, see Fig.12). As outlined above, this is biologically not plausible. The impression conveyed by the UMAP plots are confirmed numerically on the right hand side of Fig. 13. For each generated cell, we compute its nearest neighbor in the target distribution, and this way assign it a label (cell type), see App. B.2. We then obtain a cell type to cell type transition matrix, which we column-normalise (with columns containing the cell types of the generated cells), such that for each cell type, we obtain the distribution of ancestor cell types. Figure 13 shows that for the Euclidean cost, around 30% of all delta cells are derived from Ngn3 Low EP cells, while only 5% are derived from Ngn3 High EP cells. In contrast, the proportion of progenitors in Ngn3 low EP cells and Ngn3 high EP cells when using the geodesic cost is much more comparable. Similar results can be observed for alpha, beta, and epsilon cells.

Perturbation modeling with GENOT-L and U-GENOT-L For each drug, we project the single-cell RNA-seq readout of the unperturbed and perturbed cells to a 50-dimensional PCA embedding. Subsequently, we split the data randomly to obtain a train and test set with a ratio of 60%/40%. This preprocessing step holds for both the calibration score experiments

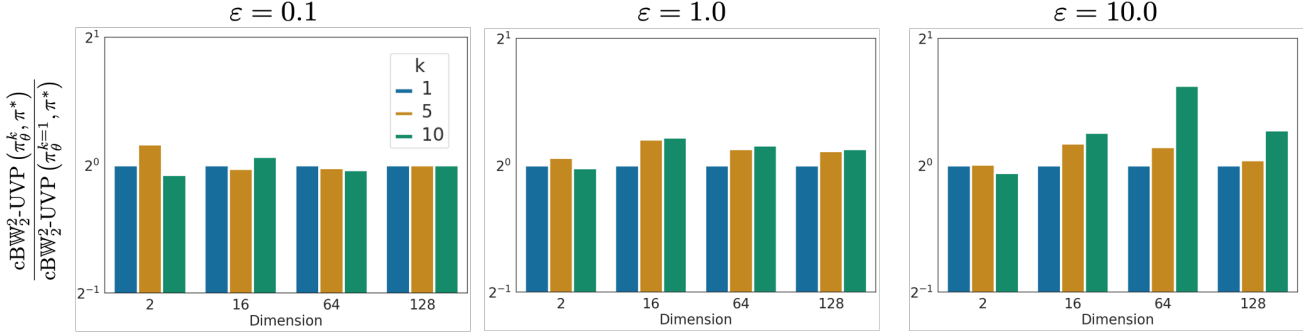


Figure 10. Evaluation of the influence of the number of data points sampled from the conditional distribution in each step, and optimally coupling noise and samples from the target distribution, see Alg. 2. $k = 1$ corresponds to the model performances reported in table 3.

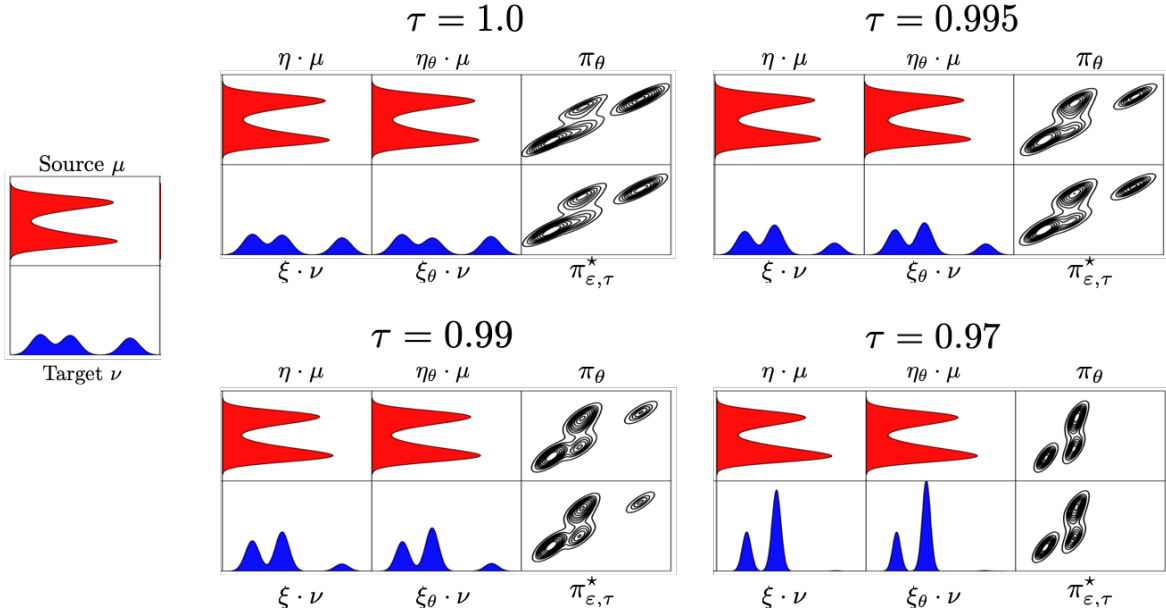


Figure 11. Unbalanced entropic neural optimal transport plan with $\epsilon = 0.05$ and varying unbalancedness parameter $\tau = \tau_1 = \tau_2$. Figure 3 shows results for $\tau = 0.98$.

and the experiments conducted with U-GENOT-L to assess the influence of unbalancedness to the accuracy score.

The uncertainty score for the calibration study is computed based on 30 samples from the conditional distribution, see appendix B.2.

In figure 15 and figure 16, we visualize the influence of unbalancedness for perturbation modeling with Dacinostat and Tanespimycin, respectively. These experiments were conducted on the full dataset for visualization reasons. While the fitting property seems to be little affected by incorporating unbalancedness (top rows), the cell type clusters are better separated for U-GENOT-L transport plans than for GENOT-L transport plans.

D.3. GENOT-Q & GENOT-F

GENOT-Q on toy data Fig. 18 visualizes the dependence of the conditional distribution on the entropy regularization parameter ϵ . In particular, we display what happens when we consider the outer coupling. Fig. 17 visualizes the density in the target space, evolving from a 2-dimensional Gaussian distribution at $t = 0$ to conditional distributions at $t = 1$. Analogously to Fig.18, we visualize the influence of the entropy regularization parameter ϵ .

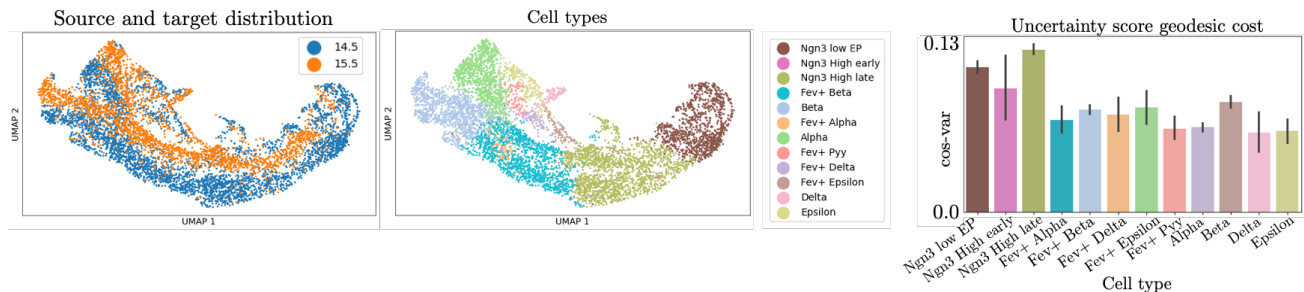


Figure 12. UMAP of the mouse pancreas development dataset colored by sample (left) and cell type (middle). We transport samples from embryonic day 14.5 to embryonic day 15.5. Uncertainty score as displayed in Fig 4 aggregated to cell type level.

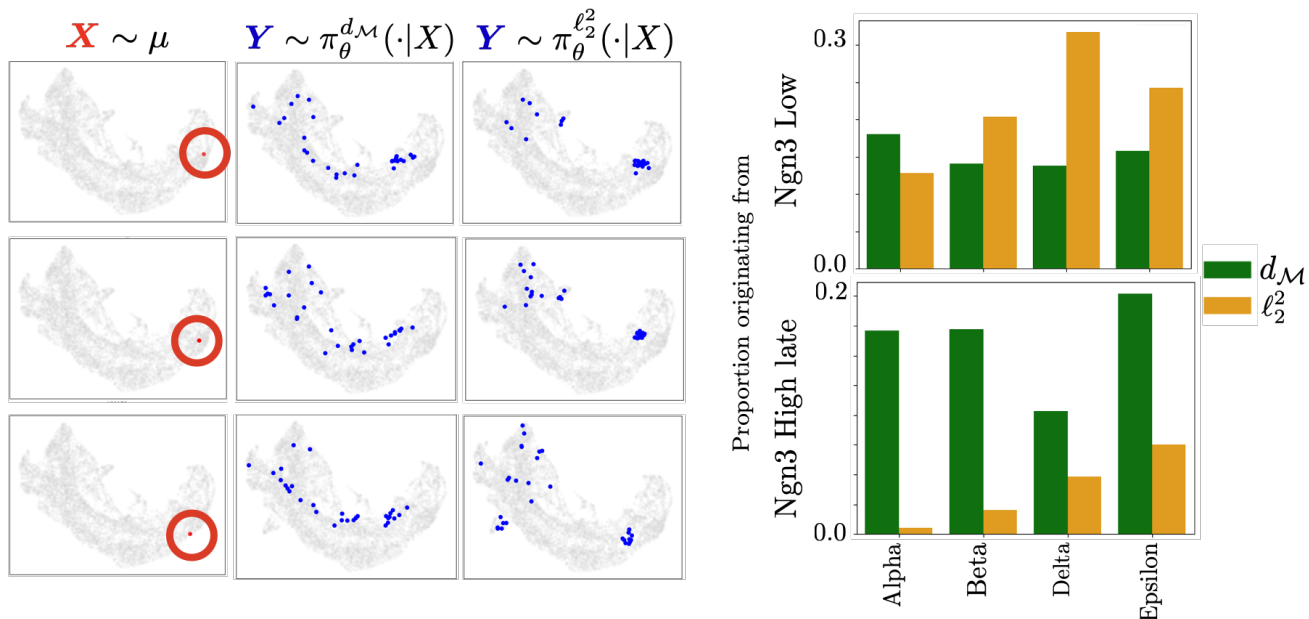


Figure 13. Left: Samples from the Ngn3 Low EP population in the leftmost column, and next to it 30 samples from their conditional distribution samples from GENOT with the geodesic cost (middle) and the squared Euclidean cost (right). Right: Proportions of alpha, beta, delta, and epsilon cells derived from the Ngn3 Low population (top) and the Ngn3 High population (bottom).

Modality translation with GENOT-Q For all experiments, we perform a random 60/40 split for training and test data. All results are reported on the test dataset. The cost matrices of all models were scaled by its mean and the entropy regularization parameter ε was set to 0.0001. Moreover, the models were trained for 5,000 iterations.

Modality translation with GENOT-F For all experiments, we perform a random 60-40 split for training and test data. All results are reported on the test dataset. The cost matrices of all models were scaled by its mean and the entropy regularization parameter ε was set to 0.001. Moreover, the models were trained for 20,000 iterations.

Figure 19 reports results of the GENOT-F model with interpolation parameters $\alpha = 0.3$ (left) and $\alpha = 0.7$ (right). While the Sinkhorn divergences are not comparable with results of the GENOT-Q model due to the respective target distributions living in different spaces, we can compare GENOT-Q with GENOT-F with respect to the FOSCTTM score. Figure 19 shows that GENOT-F strikingly outperforms GENOT-Q, hence the incorporation of the fused term is crucial for a good performance. At the same time, it is important to mention that the GW terms add valuable information to the problem setting, which can be derived from the results for GENOT-F with $\alpha = 0.3$. Here, the higher influence of the fused term causes the model to perform overall worse.

Moreover, we can visualize the optimality and fitting term in a UMAP embedding (McInnes et al., 2018). To demonstrate the robustness of our model, we train a GENOT-F model with $\varepsilon = 0.01$, $\alpha = 0.5$ and the Euclidean distance on 60% of the

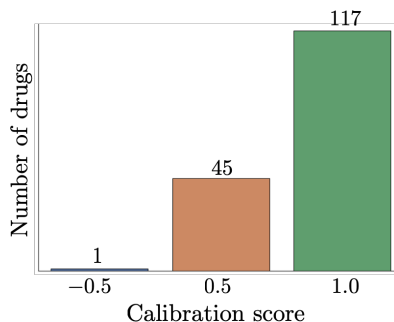


Figure 14. Calibration score for the predictions of GENOT-L for modeling cellular responses to 163 cancer drugs.

dataset (38 dimensions for the ATAC LSI embedding, 50 dimensions for the RNA PCA embedding, and 28 dimensions for the VAE embedding in the fused term) and evaluate the learnt transport plan visually. Figure 20 shows joint UMAP embeddings of predicted target and target distributions, the full legend of cell types can be found in figure 23. Qualitatively, a good mix between data points of the predicted target and the target distribution suggests a good fitting term. Optimality of the mapping can be visually assessed by considering to what extent cell types are mixed (low optimality) or separated from other cluster (high optimality).

We observed that taking the conditional mean improves results on the FOSCTTM score, but can impair the fitting property. Indeed, the mixing rate between data points belonging to the target and data points belonging to the predicted target seems to be slightly worse when considered in the joint embedding as well as when considering only the fused space and only considering the quadratic space (20).

Modality translation with U-GENOT-F To simulate a setting where there is not a match for certain cells in the target space (RNA), we remove the cells labelled as Proerythroblasts, Erythroblasts, and Normoblasts as these cells form a lineage, developing into mature Reticulocytes (not present in the dataset). Thus, they are similar in their cellular profile while being clearly distinguishable from the remaining cells. Note that this simulates an extreme setting of class imbalances, as these cells make up for more than 20% of the dataset.

While we keep the right marginals constant, as we have a true match for each cell in the target distribution, we introduce unbalancedness in the source marginals. It is important to note that the influence of the unbalancedness parameters are affected by the number of samples, as well as the entropy regularization parameter ϵ . To demonstrate the robustness of GENOT-F with respect to hyperparameters, we still choose $\alpha = 0.7$, but this time set $\epsilon = 5 \cdot 10^{-3}$. We use 50-dimensional PCA-space for the Gromov term in the RNA space, 38-dimensional LSI-space for the Gromov term in the ATAC space, and a 30-dimensional VAE-embedding for the shared space.

The computation of the growth rates for the discrete setting is described in appendix E.2. We perform a random 60-40 split to divide the data into training and test set. The FOSCTTM score only considers those cells which have a true match, i.e. cells in the source distribution belonging to the Normoblast, Erythroblast, and Proerythroblast cell types are not taken into account as their true match was removed from the target distribution.

We assess the performance w.r.t. the FOSCTTM score to ensure that the model still learns meaningful results, and consider the average reweighting function $\hat{\eta}$ per cell type (appendix D.3). We consider two values ($\tau_1 = 0.8$ and $\tau_1 = 0.3$) of the left unbalancedness parameter, while $\tau_2 = 1.0$ as for every cell in the target distribution there exists the true match in the source distribution. Tab. 4 shows that U-GENOT-F learns more meaningful reweighting functions than discrete UFGW as the average rescaling function on the left-out cell types is closer to 0, while the mean value of the rescaling function on all remaining cell types ("other") is closer to 1. At the same time, U-GENOT-F yields lower FOSCTMM scores and hence learns more optimal couplings.

Tab. 5 shows the variance across three runs, demonstrating the stability of both the learnt rescaling function as well as the performance with respect to the FOSCTTM score.

Fig. 22 shows the mean and the 95% confidence interval of the learnt growth rates per cell type. First, it is interesting to see that Normoblasts have the lowest mean of rescaling function evaluations (for both discrete UFGW and U-GENOT-F), which is due to them being most mature among the left out cell types and hence being furthest away in gene expression space /

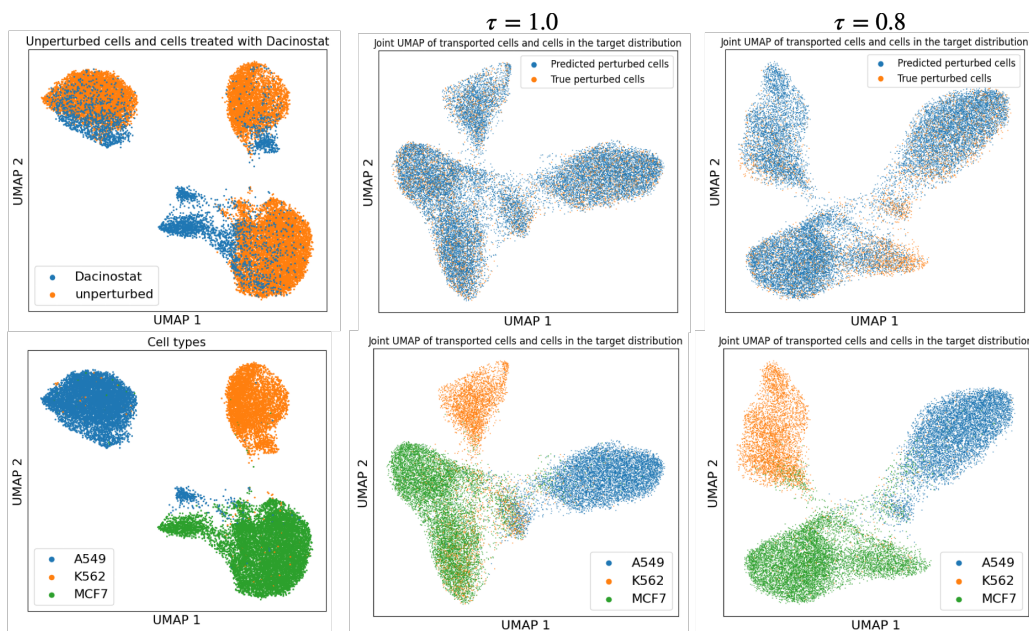


Figure 15. Visual assessment of the influence of unbalancedness in modeling cellular predictions to the cancer drug Dacinostat. In the left column, the source and target distribution are jointly plotted with cells colored by whether they belong to the source (unperturbed) or the target (perturbed) distribution (top), and which cell type they belong to (bottom). In the center column, we plot a UMAP embedding of target and predicted target distribution. The top plot colors cells according to whether a cell belongs to the target distribution or the predicted target distribution. The bottom plot is colored by cell type. The cell type of the predicted target distribution is the cell type of the pre-image of the predicted cell. The right column visualizes the same results, but this time obtained from U-GENOT-L with unbalancedness parameters $\tau = \tau_1 = \tau_2 = 0.8$.

Table 4. Mean value of the rescaling function per cluster for U-GENOT-F and discrete unbalanced FGW together with the FOSCTTM scores across three runs. Tab. 5 reports the variances for the GENOT-Q models.

model (τ_1)	Normoblast	Erythroblast	Proerythroblast	other	FOSCTTM
Discrete UFGW (0.8)	0.788	0.820	0.842	0.945	0.258
U-GENOT-F (0.8)	0.622	0.733	0.894	1.077	0.131
Discrete UFGW (0.3)	0.591	0.586	0.734	0.761	0.311
U-GENOT-F (0.3)	0.295	0.430	0.554	1.186	0.162

ATAC space from the common origin of all cells, the HSC cluster. Moreover, it is obvious that the 95% confidence interval of the reweighting function (across cells in one cell type) is much smaller for U-GENOT-F than for discrete UFGW. This is desirable as cells within one cell type are very similar in their ATAC profile.

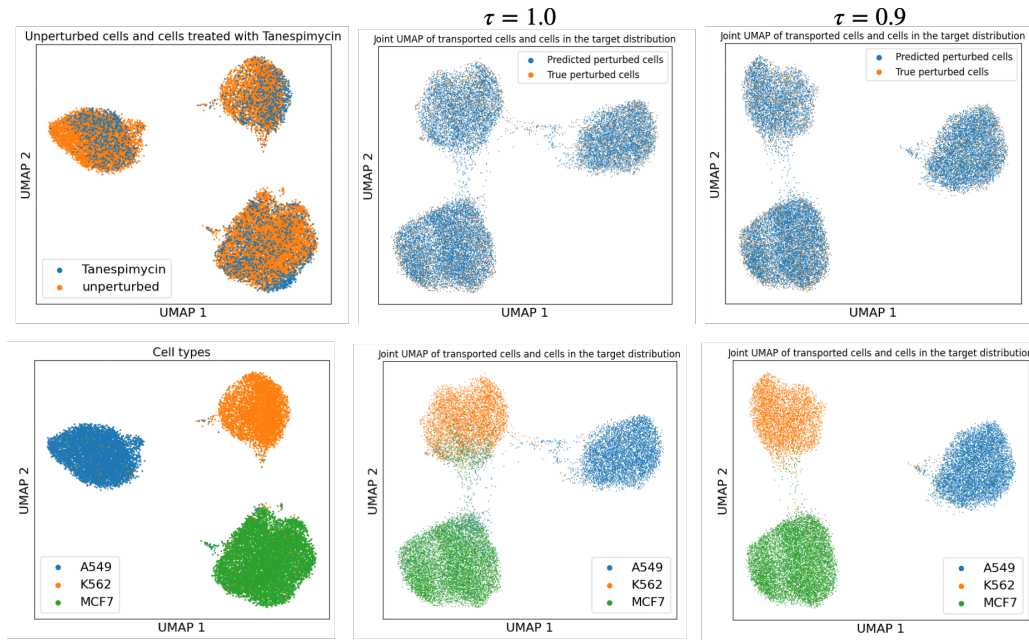


Figure 16. Visual assessment of the influence of unbalancedness in modeling cellular predictions to the cancer drug Tanespimycin. In the left column, the source and target distribution are jointly plotted with cells colored by whether they belong to the source (unperturbed) or the target (perturbed) distribution (top), and which cell type they belong to (bottom). In the center column, we plot a UMAP embedding of target and predicted target distribution. The top plot colors cells according to whether a cell belongs to the target distribution or the predicted target distribution. The bottom plot is colored by cell type. The cell type of the predicted target distribution is the cell type of the pre-image of the predicted cell. The right column visualizes the same results, but this time obtained from U-GENOT-L with unbalancedness parameters $\tau = \tau_1 = \tau_2 = 0.9$.

Table 5. Comparison of reweighting functions learnt by U-GENOT-F and discrete unbalanced FGW model (τ_1)

model (τ_1)	Normoblast	Erythroblast	Proerythroblast	other	FOSCTTM
U-GENOT-F (0.8)	$3 \cdot 10^{-6}$	$2 \cdot 10^{-5}$	$1 \cdot 10^{-4}$	$5 \cdot 10^{-5}$	$3 \cdot 10^{-5}$
U-GENOT-F (0.3)	$2 \cdot 10^{-6}$	$9 \cdot 10^{-6}$	$5 \cdot 10^{-4}$	$8 \cdot 10^{-4}$	$9 \cdot 10^{-5}$

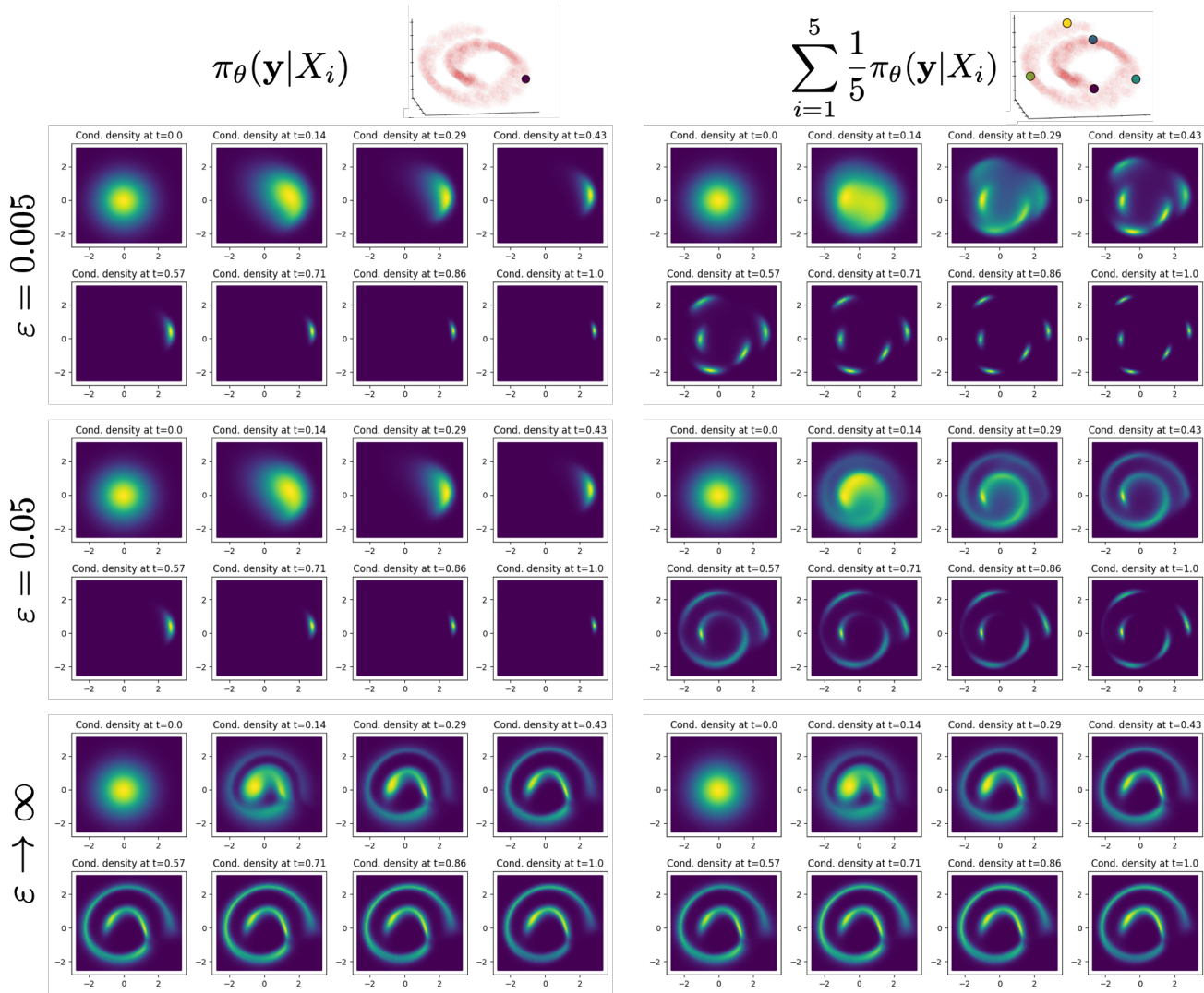


Figure 17. Evolution of the density from $t = 0$ corresponding to the latent distribution (i.e. multivariate standard Gaussian distribution) to $t = 1$ corresponding to the density of the conditional distribution $\pi_{\theta}(\mathbf{y}|X_i)$. The setup is the same as in figure 6, in effect we transport a three-dimensional Swiss roll to a two-dimensional spiral. The left panel displays the densities of *one* conditional distribution, while the right panel visualizes a mixture of densities over time. The top part of the figure corresponds to GENOT-Q models with entropy regularization parameter $\varepsilon = 0.005$, while the middle ones correspond to $\varepsilon = 0.005$. The bottom ones correspond to the outer coupling. The markers on the 3-dimensional plot on the very top correspond to data points in the source distribution.

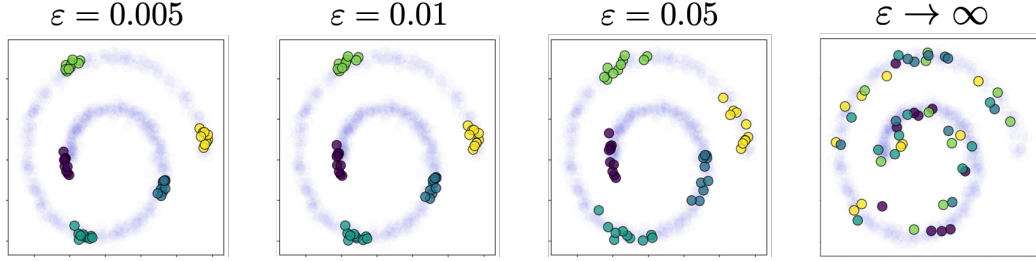


Figure 18. Samples from conditional distributions $\pi_\theta(\cdot|\mathbf{x})$ for GENOT-Q models trained with different entropy regularization parameters ε . The setup is the same as in figure 6, in effect we transport a three-dimensional Swiss roll to a two-dimensional spiral, which is colored in blue (with high transparency). The right plot shows the result when choosing the outer coupling as opposed to an EOT coupling. The source distribution as well as the data points which are conditioned on are visualized in figure 6.

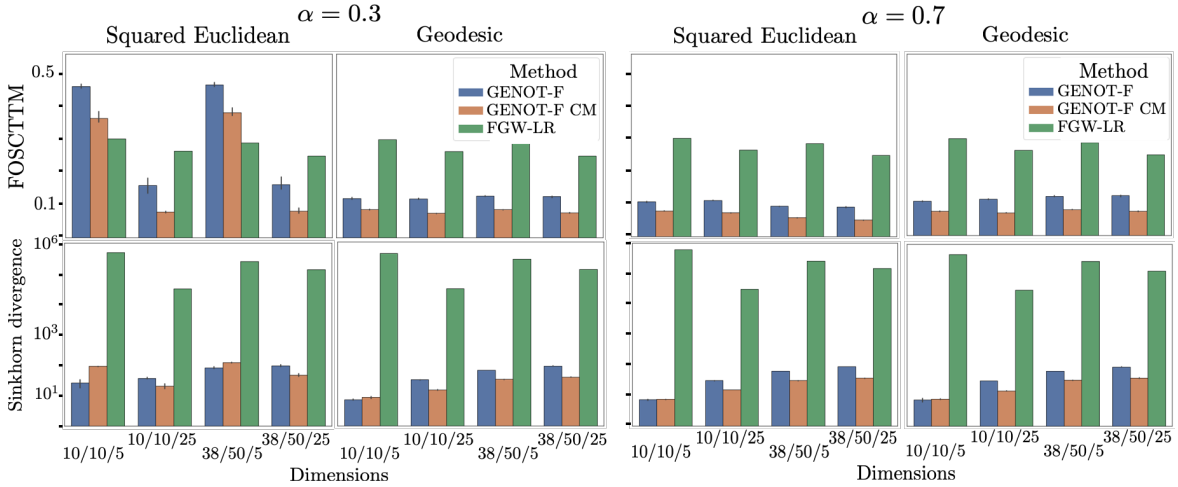


Figure 19. Mean and 95% confidence interval (across three runs) of the FOSCTTM score (top) and the Sinkhorn divergence (bottom) of GENOT-F and discrete FGW with linear regression for out-of-sample estimation. Experiments are categorized by the numbers $d_1/d_2/d_3$, where d_1 is the dimension of the space corresponding to the GW of the source distribution, d_2 is the dimension of the space corresponding to the GW of the target distribution, and d_3 is the dimension of the shared space. Results are reported for the interpolation parameter $\alpha = 0.3$ (left half) and $\alpha = 0.7$ (right half).

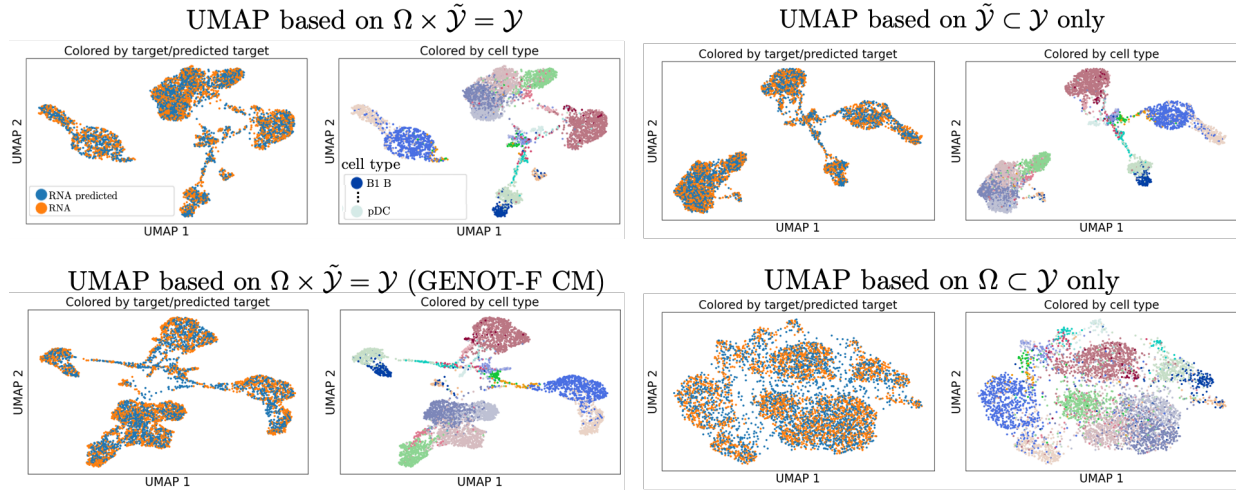


Figure 20. UMAP embedding of target and predicted target based on subspaces of the target domain. Top left: full target space. Top right: incomparable space only. Bottom left: full target space (with predicted target computed by the mean of the conditional distributions). Bottom right: share space only. Cells are colored based on whether they belong to the target distribution or the predicted target distribution in the left plot of each subplot. Cells are colored based on their cell type in the right plot of each subplot. For cells which belong to the predicted target distribution, the cell type is defined as the cell type of the preimage. Shown are results on the test data set, corresponding to 40% of the full dataset.

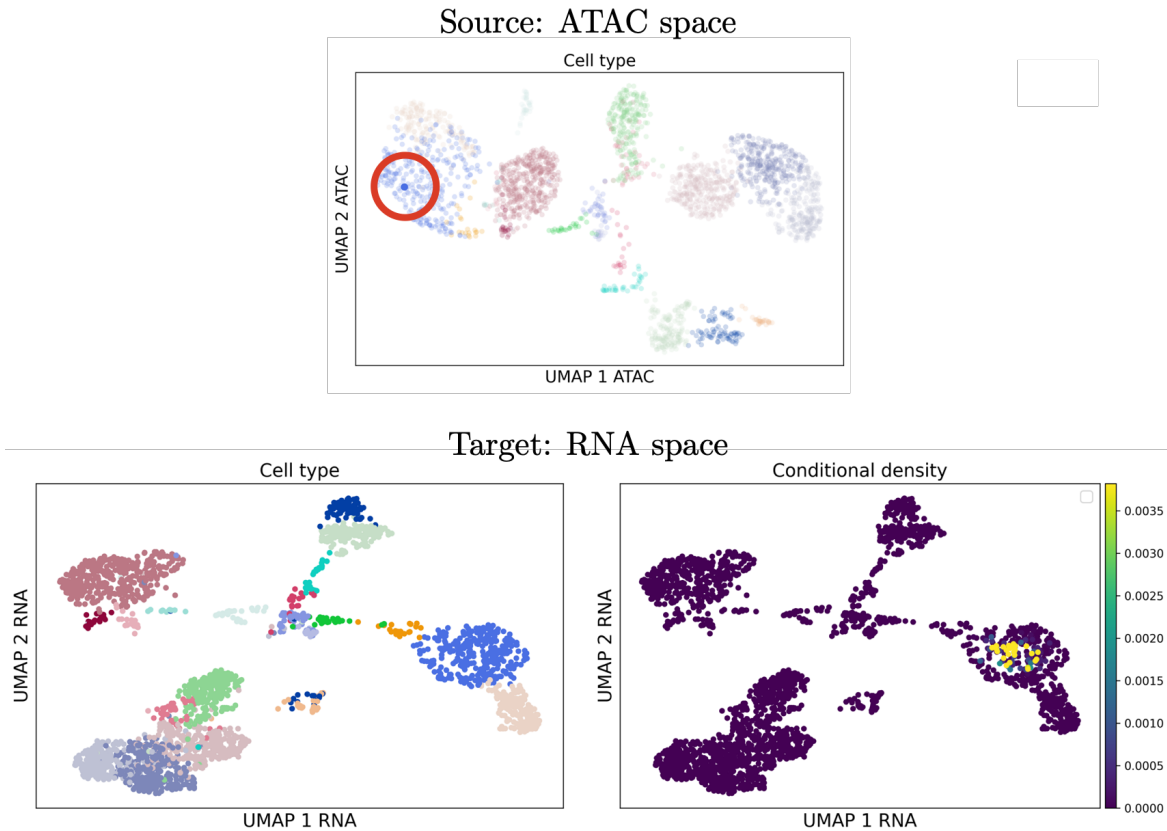


Figure 21. Top: A single Erythroblast cell is highlighted while all other cells in the source distribution are depicted with increased transparency. Bottom: Target distribution colored by cell type (left) and colored by the conditional density (conditioned on the highlighted cell above) evaluated on all cells in the target distribution. All cells with a relatively high density belong to the Erythroblast cluster, hence the mapping learnt by GENOT-F is meaningful.

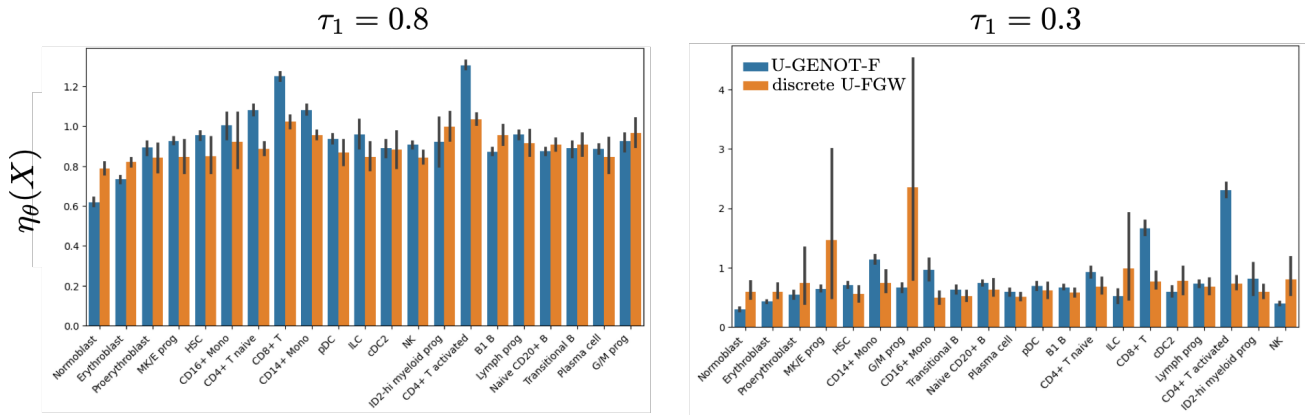


Figure 22. Comparison of learnt growth rates of discrete UFGW and U-GENOT-F aggregated to cell type level for unbalancedness parameters $\tau_1 = 0.8, \tau_2 = 1$ (left) and $\tau_1 = 0.3, \tau_2 = 1$ (right).

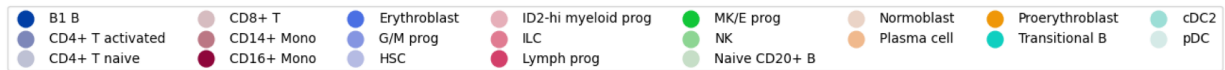


Figure 23. Complete legend of cell types for Fig. 7, Fig. 20 and Fig.21.

E. Competing methods

E.1. EOT benchmark in the balanced, linear case

As results for competing methods were taken from Gushchin et al. (2023), we refer to the original publication for details on the competing methods.

E.2. Regression for out-of-sample data points

Out-of-sample prediction for GW has been considered in (Alvarez-Melis & Jaakkola, 2018). Yet, their methods rely on an orthogonal projection, which only works if both the sample size and the feature dimensions are the same in both spaces. Hence, we rely on a barycentric projection for in-sample data points. For out-of-sample data points we project a data point onto the training set and apply the barycentric projection to the linear combination of points in the in-sample distribution. Let $\mathbf{X} \in \mathbb{R}^{n \times d}$ be the matrix containing n in-sample data points.

Then, for a data point in the source distribution $\mathbf{x} \in \mathbb{R}^d$, let

$$\hat{\beta}_{\mathbf{x}} = \arg \min_{\beta \in \mathbb{R}^n} \|\hat{\mathbf{x}} - \mathbf{X}^T \beta\|_2^2 \quad (37)$$

where the sum is taken over the n in-sample data points. Moreover, let $p_i = \sum_{j=1}^m \Pi_{ij}$. Then, the barycentric projection of a point in the source distribution is given as

$$\hat{\mathbf{y}} = \sum_{i=1}^n \frac{\hat{\beta}_i}{p_i} \sum_{j=1}^m \Pi_{ij} \mathbf{y}_j \in \mathcal{Y}. \quad (38)$$

Similarly, we can apply this procedure to estimate rescaling factors in the unbalanced setting. To ensure non-negativity of the rescaling function, we perform regression with non-negative weights:

$$\hat{\alpha}_{\mathbf{x}} = \arg \min_{\alpha \in \mathbb{R}_{\geq 0}^n} \|\hat{\mathbf{x}} - \mathbf{X}^T \alpha\|_2^2 \quad (39)$$

To estimate the rescaling function for a data point \hat{x} , the estimated left rescaling function is given as

$$\hat{\eta} = \sum_{i=1}^n \hat{\alpha}_i \eta_i \in \mathbb{R} \quad (40)$$

where $\{\eta_i\}_{i=1}^n$ is the set of reweighting function evaluations of in-sample data points.

F. Implementation

The GENOT framework is implemented in JAX (Bradbury et al., 2018). We use the discrete OT solvers provided by OTT-JAX (Cuturi et al., 2022).

F.1. Parameterization of the vector field

The vector field is parameterized with a feed-forward neural network which takes as input the time (which is cyclically encoded with frequency 128), the condition (i.e. the samples from the source distribution) and the latent noise. Each of these input vectors are independently embedded by one block of layers before the embeddings are concatenated and applied to another block of layers, followed by one output layer. If not stated otherwise, one block of layers consists of 8 layers of width 256 with *silu* activation functions.

F.2. Parameterization of the rescaling functions

Rescaling functions are parameterized as feed-forward neural networks with 5 layers of width 128, followed by a final *softplus* activation function to ensure non-negativity.

F.3. Training details

We report default values for the different parameters of the GENOT Alg.1. If not stated otherwise in the corresponding experiments section, we use these parameters. As in Alg.1, parameters related to U-GENOT are provided in teal.

- **Batch size:** $n = 1024$.
- **Entropic regularization strength:** $\varepsilon = 10^{-2}$. By default, we do not scale the cost matrices passed to discrete OT solvers.
- **Unbalancedness parameter:** $\tau = (1, 1)$. This means that by default, we impose the hard marginal constraints.
- **Number of training iterations:** $T_{\text{iter}} = 10,000$.
- **Optimizer:** AdamW with **learning rate** $\text{lr} = 10^{-4}$, and **weight decay** $\lambda = 10^{-10}$. This is used for both, the vector field $v_{t,\theta}$, and the re-weighting functions η_θ, ξ_θ .

When using the graph distance, we construct a k-nearest neighbor graph with *batch_size* number of edges. Then we apply a softmax to obtain connectivities from the distances in the knn-graph. For the approximation of the heat kernel, we use the default parameters provided by the implementation in OTT-JAX (Cuturi et al., 2022).